Low-mass galaxy assembly in simulations: regulation of early star formation by radiation from massive stars

Trujillo-Gomez, Sebastian; Klypin, Anatoly; Colin, Pedro; Ceverino, Daniel; Arraki, Kenza; Primack, Joel

Abstract: Despite recent success in forming realistic present-day galaxies, simulations still form the bulk of their stars earlier than observations indicate. We investigate the process of stellar mass assembly in low-mass field galaxies, a dwarf and a typical spiral, focusing on the effects of radiation from young stellar clusters on the star formation (SF) histories. We implement a novel model of SF with a deterministic low efficiency per free-fall time, as observed in molecular clouds. Stellar feedback is based on observations of star-forming regions, and includes radiation pressure from massive stars, photoheating in H II regions, supernovae and stellar winds. We find that stellar radiation has a strong effect on the formation of low-mass galaxies, especially at z 1, where it efficiently suppresses SF by dispersing cold and dense gas, preventing runaway growth of the stellar component. This behaviour is evident in a variety of observations but had so far eluded analytical and numerical models without radiation feedback. Compared to supernovae alone, radiation feedback reduces the SF rate by a factor of˜100 at z 2, yielding rising SF histories which reproduce recent observations of Local Group dwarfs. Stellar radiation also produces bulgeless spiral galaxies and may be responsible for excess thickening of the stellar disc. The galaxies also feature rotation curves and baryon fractions in excellent agreement with current data. Lastly, the dwarf galaxy shows a very slow reduction of the central dark matter density caused by radiation feedback over the last˜7 Gyr of cosmic evolution.

DOI: https://doi.org/10.1093/mnras/stu2037

Monthly Notices
of the
ROYAL ASTRONOMICAL SOCIETY

MNRAS **446,** 1140–1162 (2015) doi:10.1093/mnras/stu2037

Low-mass galaxy assembly in simulations: regulation of early star formation by radiation from massive stars

Sebastian Trujillo-Gomez,[1]★ Anatoly Klypin,[1] Pedro Colín,[2] Daniel Ceverino,[3] Kenza S. Arraki[1] and Joel Primack[4]

[1]*Astronomy Department, New Mexico State University, Las Cruces, NM 88003, USA*
[2]*Centro de Radioastronomia y Astrofísica. Universidad Nacional Autónoma de México, A.P. 72-3 (Xangari), Morelia, Michoacán 58089, México*
[3]*Departamento de Física Teórica, Universidad Autónoma de Madrid, E-28049 Madrid, Spain*
[4]*Department of Physics, University of California at Santa Cruz, Santa Cruz, CA 95064, USA*

Accepted 2014 September 29. Received 2014 September 17; in original form 2013 December 1

ABSTRACT

Despite recent success in forming realistic present-day galaxies, simulations still form the bulk of their stars earlier than observations indicate. We investigate the process of stellar mass assembly in low-mass field galaxies, a dwarf and a typical spiral, focusing on the effects of radiation from young stellar clusters on the star formation (SF) histories. We implement a novel model of SF with a deterministic low efficiency per free-fall time, as observed in molecular clouds. Stellar feedback is based on observations of star-forming regions, and includes radiation pressure from massive stars, photoheating in H II regions, supernovae and stellar winds. We find that stellar radiation has a strong effect on the formation of low-mass galaxies, especially at $z > 1$, where it efficiently suppresses SF by dispersing cold and dense gas, preventing runaway growth of the stellar component. This behaviour is evident in a variety of observations but had so far eluded analytical and numerical models without radiation feedback. Compared to supernovae alone, radiation feedback reduces the SF rate by a factor of $\sim$100 at $z \lesssim 2$, yielding rising SF histories which reproduce recent observations of Local Group dwarfs. Stellar radiation also produces bulgeless spiral galaxies and may be responsible for excess thickening of the stellar disc. The galaxies also feature rotation curves and baryon fractions in excellent agreement with current data. Lastly, the dwarf galaxy shows a very slow reduction of the central dark matter density caused by radiation feedback over the last $\sim$7 Gyr of cosmic evolution.

Key words: stars: formation – galaxies: dwarf – galaxies: evolution – galaxies: formation – cosmology: theory – dark matter.

1 INTRODUCTION

In the last few years, the Λ cold dark matter (ΛCDM) cosmological paradigm has been extensively and successfully tested at various scales and now provides a well-defined framework in which to study the process of galaxy formation. As observations of galaxies become more detailed and reach farther into the past, the theory is confronted with a large number of constraints both at present and at high redshift. Cosmological simulations of individual galaxies have only very recently reached the level of detail and resolution necessary to properly include the physical processes that shape galaxies. Although it now seems possible to fine-tune physical models to produce individual simulated galaxies that resemble the Milky Way (MW) and present-day dwarfs (e.g. Governato et al. 2010; Brook et al. 2011; Guedes et al. 2011; Shen et al. 2014), much progress is yet to come in our understanding of galaxy formation. Two essential properties of galaxies are absent from numerical models (see, however, Brook et al. 2012). First, the observed fraction of the universal baryons that condense to form stars in galaxies is very small and has a steep mass dependence (e.g. Trujillo-Gomez et al. 2011). Secondly, there is a sharp contrast between the growth of dark matter (DM) haloes and the growth of galaxies within them (Weinmann et al. 2012). Observational estimates of the stellar mass growth of galaxies show that low-mass galaxies formed most of their stars recently, while massive ones assembled a large fraction of their stellar mass at high redshift (e.g. Salim et al. 2007; Firmani & Avila-Reese 2010; Leitner 2012; Behroozi, Wechsler & Conroy 2013; Moster, Naab & White 2013).

Several lines of evidence including lensing, satellite kinematics and semi-empirical models indicate that galaxy formation is a very inefficient process, where most of the cosmological baryons (i.e.

★E-mail: st@astronomy.nmsu.edu

the primordial gas) do not condense into galaxies (e.g. Fukugita, Hogan & Peebles 1998; Hoekstra et al. 2005; Mandelbaum et al. 2006; Jiang & Kochanek 2007; Behroozi, Conroy & Wechsler 2010; Guo et al. 2010; Trujillo-Gomez et al. 2011; Leauthaud et al. 2012; Rodriguez-Puebla, Drory & Avila-Reese 2012). Previous works have outlined the need for efficient stellar feedback to expel gas from galaxies. However, this process should have a strong mass dependence in order to reproduce the observed cold baryon fractions of all galaxies. A dependence of the baryon fraction on morphology has also been suggested (e.g. Dutton et al. 2010; Trujillo-Gomez et al. 2011). After decades of producing galaxies with too many stars, several simulations have recently succeeded at matching observed stellar masses (e.g. Guedes et al. 2011; Munshi et al. 2013; Di Cintio et al. 2014). These typically rely on increasing the effect of supernovae (SNe) feedback by boosting the energy yield or by extending the disipationless phase of the expansion to several million years at the scales of molecular clouds. However, it is uncertain whether these large superheated bubbles actually occur in nature.

As observations of the high-redshift Universe improved, it was realized that simulated galaxies assemble their stars much earlier than evidence suggests. Studies of the assembly of the stellar component of galaxies have found evidence of the phenomenon termed 'downsizing'. Direct measurements of the specific star formation rates (sSFRs) in dwarf galaxies indicate that they increase with decreasing stellar mass, both at present and out to $z \sim 2$ (e.g. Baldry et al. 2004; Noeske et al. 2007; Salim et al. 2007; Rodighiero et al. 2010; Karim et al. 2011; Whitaker et al. 2012). Stellar mass growth tracks obtained from semi-empirical models also produce sSFRs that are higher for lower mass galaxies (Firmani & Avila-Reese 2010; Behroozi et al. 2013). This implies that dwarfs assembled their stellar component later than massive galaxies, and the smaller their mass, the greater the delay (e.g. Firmani & Avila-Reese 2010; Avila-Reese et al. 2011). Avila-Reese et al. (2011), De Rossi et al. (2013) and (González-Samaniego et al. 2014) show that cosmological galaxy formation simulations that include only SNe feedback are incapable of producing rising star formation (SF) histories in dwarfs, even when strong outflows are imposed. In addition, Firmani, Avila-Reese & Rodríguez-Puebla (2010) show that seminumerical models of disc formation with outflows and re-accretion that are tuned to reproduce the present-day stellar-mass–halo mass relation give rise to an increasing sSFR as a function of mass, opposite to the observed trend. This problem is also present in semi-analytic models (e.g. Somerville et al. 2008), which obtain a population of dwarf galaxies that is old and quenched. This problem is not limited to low-mass haloes. Fine-tuned simulations of MW-like galaxies also form most of their stars at high redshift. For instance, the *Eris2* simulation is intended to reproduce the MW at present but has a stellar mass $M_* = 1.5 \times 10^{10}\,\mathrm{M}_\odot$ already in place at $z = 3$ (Shen et al. 2013). This is more than 10 times larger than in the observational inferences (e.g. Behroozi et al. 2013; Moster et al. 2013). Clearly, the models currently lack a mechanism to decouple the galaxy growth from the DM halo growth (Weinmann et al. 2012).

Recently, forms of feedback that are fundamentally different from SNe have been shown to be essential to galaxy formation. Murray, Quataert & Thompson (2010) analysed the dynamical effects of several forms of stellar feedback on parent molecular clouds. In their models they include momentum input from ionized gas in H II regions, shocked stellar winds, hot gas pressure, protostellar jets and cosmic rays. Murray et al. (2010) conclude that radiation pressure (RP) on dust grains is likely to be the dominant form of feedback in star-forming galaxies. A variety of other studies have reached the same conclusions, placing the combination of RP and photoionization of gas by massive stars as the dominant mechanism for disruption of molecular clouds and internal regulation of the SF process (Indebetouw et al. 2009; Krumholz & Matzner 2009; Murray et al. 2010; Andrews & Thompson 2011; Hopkins, Quataert & Murray 2011; Lopez et al. 2011; Pellegrini, Baldwin & Ferland 2011). RP alone might also be the only mechanism that explains galactic fountains and the warm gas outflows observed in absorption in high-redshift galaxies (Murray, Ménard & Thompson 2011). In addition, recent numerical work by Krumholz & Thompson (2012) shows that radiation feedback fully accounts for the large gas velocity dispersions measured in young star clusters in the MW. There are at least three reasons why radiative feedback is an essential ingredient of the galaxy formation process. First, observations show that molecular clouds begin to disperse shortly after the O stars form and before the first SNe explode and deposit their energy into the gas (Kawamura et al. 2009). Secondly, the total energy output of a stellar cluster is dominated by radiation. The rate of radiative energy output by O and B stars is ∼200 times larger than the average power injected by SNe and stellar winds during the lifetime of the most massive stars. Thirdly, it is difficult to explain the large gas turbulence values observed in star-forming regions without including the momentum input by radiation (Murray et al. 2010).

There have been few attempts to incorporate RP from young stellar clusters in numerical models of galaxy formation. In most cases, the effect of radiation is crudely modelled as a simple increase in the thermal energy output of massive stars (similar to SNe thermal feedback; Brook et al. 2011; Macciò et al. 2012) or by imparting kinetic energy to the gas while temporarily decoupling it from hydrodynamic forces (e.g. Oppenheimer & Davé 2008; Oppenheimer et al. 2010; Genel et al. 2012). In the most detailed approach, Hopkins et al. (2011) performed high resolution smoothed particle hydrodynamics (SPH) simulations of isolated galaxy models to follow the effects of RP using self-consistent star cluster identification and optical depth calculation. They show that radiative feedback may be the mechanism responsible for controlling the amount of gas available for SF in a manner that becomes independent of the sub-grid SF parameters. In their isolated models this resulted in a drastic reduction of the SF efficiency.

Hopkins et al. (2011) show that simulated isolated galaxies can self-regulate their SF with radiative feedback alone, without the need for SN explosions. In a recent paper, Ceverino et al. (2014) include the effect of RP and photoionization from UV photons in cosmological simulations of a high-redshift MW progenitor. Their simulations with radiation feedback show a reduction of the star formation rate (SFR) by a factor of ∼2–3 at $z = 3$ compared to a simulation with SNe energy alone, with radiation momentum playing the dominant role and gas photoionization having only a secondary effect. These works point towards a new paradigm of galaxy formation, where radiation from massive stars is responsible for regulating SF and powering galactic winds, while the properties of the inter-stellar medium (ISM) are controlled by the energy from SNe.

In this paper, we use cosmological simulations with a new, realistic SF model and radiative feedback from massive stars to investigate the assembly of baryons in low-mass galaxies. Unless specified otherwise, we employ the term 'radiative feedback' to refer to both the effect of scattering of stellar radiation by gas and dust, and to the thermal pressure of gas that is photoionized by stellar UV photons. Here on we use the term 'RP' to denote only the pressure due to scattering of photons on gas and dust. The paper is organized as follows. Section 2 describes the code and the new model of SF and feedback and Section 3 shows estimates of the effects of feedback

on star-forming gas. Section 4 summarizes the properties of the simulations and Section 5 presents our results. In Section 6 we summarize our results.

2 PHYSICAL MODEL

To perform our simulations, we used the adaptive mesh refinement *N*-body+hydrodynamics code HYDROART (Kravtsov, Klypin & Khokhlov 1997; Kravtsov 1999). The code is adaptive in both space and time, achieving higher resolution in regions of higher mass density. The physical model in the code includes many relevant physical processes such as cooling due to metals and molecules down to 300 K, a homogeneous ultraviolet (UV) background, gas self-shielding, as well as advection of metals. We now describe the motivation and implementation of the processes of SF and feedback.

2.1 Stellar feedback

Our stellar feedback model includes contributions from four dominant terms: RP, photoionization heating, Type II SNe (SNeII) and shocked stellar winds.

Radiation pressure. The treatment of stellar RP follows Murray et al. (2010), Hopkins et al. (2011), Agertz et al. (2013) and Ceverino et al. (2014), where the total momentum of the radiation field (in the form of UV and optical photons),

$$\dot{p}_{\rm rad}(t) = \frac{L(t)}{c}, \tag{1}$$

is coupled to the gas and dust as a result of scattering and/or absorption. Fig. 1 shows the total luminosity output from a burst of SF obtained using STARBURST99 (Leitherer et al. 1999). During the initial 40 Myr, the total energy radiated by a star cluster is 1.8×10^{50} erg $M_{\odot}{}^{-1}$, or about 10 times larger than the mechanical energy released by SNe and stellar winds. The total momentum of the radiation couples to the gas through two separate processes. Initially, a photon of any wavelength may be scattered or absorbed by an atom. In addition, UV and optical photons may also be absorbed by dust. If a photon is absorbed by a dust grain, it will be re-emitted as a lower energy infrared photon. Depending on the density structure of the star-forming cloud, and on the optical depth of dust in the infrared, the photon may be absorbed and re-emitted multiple times. Through collisions between atoms and grains, this process will enhance the amount of momentum transferred to the star-forming cloud. Thus, the total momentum imparted to the gas will be

$$\dot{p}(t) \approx (1 - {\rm e}^{-\tau_{\rm UV}} + \tau_{\rm IR}) \frac{L(t)}{c}. \tag{2}$$

Because the gas immediately surrounding a newly formed star cluster reaches high densities, and dust is an efficient absorber of UV photons, we assume $1 - \exp(-\tau_{\rm UV}) \approx 1$. The effect of radiation momentum on the gas will vanish once the expanding gas shell grows larger than the size of a giant molecular cloud and its optical depth decreases (Murray et al. 2010).

There is some debate in the literature over the value of the infrared optical depth of the gas due to dust. While $\tau_{\rm IR}$ can reach large values (∼50–100) in galaxy models without radiative transfer (Murray et al. 2010; Hopkins et al. 2011), self-regulation seems to make the properties of the ISM nearly independent of the strength of the radiative forcing. However, in simplified radiation hydrodynamics simulations, Krumholz & Thompson (2012) find that although there is enough momentum in the radiation field, once the radiation pushes on the gas strongly enough for radiative Raleigh–Taylor instabilities to set in, radiation becomes dynamically ineffective and the Eddington ratio of the gas saturates at unity. They obtain modest values $1 < \tau_{\rm IR} < 10$. Most recently, Davis et al. (2014) show that using a more accurate radiative transfer approximation allows the radiation to be trapped, resulting in large optical depths that scale linearly with the column density estimated without radiative transfer. The local metallicity of the gas is also expected to affect the dust content and hence its absorption properties. Due to the current uncertainty in the optical depth $\tau_{\rm IR}$, we explore a broad range of values in our numerical experiments.

Photoionization heating. In addition to imparting momentum through scattering, UV radiation ionizes the gas surrounding a young cluster, creating an H II region. The observed extent of *evolved* H II regions ranges from ∼10–100 pc, with temperatures of $\sim 10^4$ K, and densities 50–1000 cm^{-3} (Lopez et al. 2014). Thus, the thermal pressure of gas due to photoionization within the H II region is $P/k_B \sim 10^6$–10^7 K cm^{-3} a few million years after the first massive stars form (Lopez et al. 2014). However, the density of ionized gas is expected to be higher at the time of formation of the first O and B stars and thus the thermal pressure should be considerably larger during the initial stages.[1] Since the region is overpressured with respect to its surrounding gas, it will expand and become rarefied, causing a decrease in the thermal gas pressure with time.

Very few galaxy formation simulations, including those that attempt a full accounting of stellar feedback (e.g. Agertz et al. 2013;

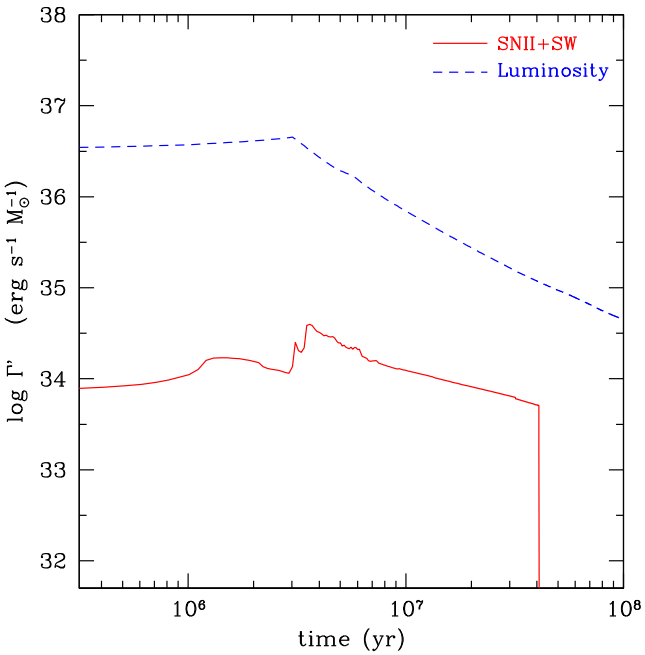

Figure 1. Specific power output by a single burst of SF as a function of time as calculated by STARBURST99. The dashed line shows the specific stellar luminosity per unit stellar mass, while the solid line is the specific mechanical power from SNeII and stellar winds. The radiative energy is at least 200 times larger than the combined energy from SN explosions and stellar winds during the initial ∼3 Myr and declines quickly thereafter. Most galaxy formation simulations do not include this contribution to stellar feedback.

[1] Ultracompact H II regions are thought to be the progenitors of evolved H II regions. They are much more compact and dense than their evolved counterparts, with $n \gtrsim 10^5$ cm^{-3} (Hoare et al. 2007).

Hopkins et al. 2014), include the extra pressure from photoheating explicitly. However, in high-resolution simulations of SF in isolated molecular clouds, Dale, Ercolano & Bonnell (2012) and Colín, Vázquez-Semadeni & Gómez (2013) find that ionization heating alone is sufficient to destroy massive clouds and to regulate the SF efficiency.

SNe and stellar winds. As is commonly done in simulations of galaxy formation, we include the mechanical energy from unresolved SNeII shockwaves and shocked stellar winds. Following the model in (Ceverino, Dekel & Bournaud 2010), this energy is injected in the gas as thermal energy. As Fig. 1 shows, there is a 3 Myr delay after the formation of a cluster and before the first SNe explode. During this period, stellar winds provide an amount of power equivalent to the SNII contribution. In addition, the contribution of SNeIa is modelled as an injection of thermal energy with a broad distribution in time that peaks at a stellar age of 1 Gyr. Since the energy deposition rate is about 3 orders of magnitude smaller than the SNII contribution, it should be dynamically unimportant for galaxies with ongoing SF.

We implement each feedback component in the code as follows.

(1) The rate of momentum injection from the radiation field into the gas is

$$\dot{p}_{\rm rad}(t) \equiv \tau_{\rm tot} \frac{L(t)}{c}, \tag{3}$$

where $\tau_{\rm tot} \equiv 1 + \tau_{\rm IR}$, and $L(t)$ is the total luminosity of the star cluster as a function of time estimated using STARBURST99 for a Chabrier initial mass function (IMF). Assuming conservation of momentum, we obtain the pressure on the surrounding gas by computing the momentum flux through the cell interface:

$$P_{\rm rad}(t) = \eta \frac{\dot{p}_{\rm rad}(t)}{6\Delta x^2}, \tag{4}$$

where the term $6\Delta x^2$ is the surface area of the cell where the stellar particle is located. We set the parameter $\eta = 3$ to approximately match the correction used by Agertz et al. (2013), which accounts for numerical momentum loss when a star particle moves across grid cells. In general, the model is independent of resolution since by construction the total momentum of the radiation is conserved as it flows out of the cell. A detailed discussion of convergence of the model can be found in Ceverino et al. (2014). We adopt the initial specific radiant energy injection rate $L_0/M_* = 3.66 \times 10^{36}\,{\rm erg\,s^{-1}\,M_\odot}^{-1}$, and a time dependence modelled as shown in Fig. 1. We assume a fixed value $\tau_{\rm UV} = 1$ wherever gas has the conditions for stars to form. The RP is added as a non-thermal pressure in every star-forming cell until the gas density in the cell drops below a fixed threshold value, $n_{\rm th}$. Since our typical resolution limits the highest gas density in SF regions, we cannot estimate the optical depth directly using the column density of the gas. Instead, we select a fixed $\tau_{\rm IR}$ for each simulation run. The values are selected to span the range of estimates in the literature.

(2) The dynamical effect of heating due to photoionization (i.e. photoheating) is included by adding an extra non-thermal pressure to the cell containing the young stellar particle during the initial $\sim$1 Myr of the lifetime of the particle. The fiducial value of this pressure is chosen to be $P_{\rm PH,\,0}/{\rm k}_B = 10^6\,{\rm K\,cm^{-3}}$ in the initial 100 kyr and rapidly declines to $\sim 10^4\,{\rm K\,cm^{-3}}$ after 800 kyr to mimic the drop in density as the H II region grows. The time dependence is modelled as

$$P_{\rm PH}(t) = \begin{cases} P_{\rm PH,0} & \text{for} \quad t \le 100\,{\rm kyr}, \\ \frac{P_{\rm PH,0}}{(t/100\,{\rm kyr})^{2.5}} & \text{for} \quad 100\,{\rm kyr} < t < 1\,{\rm Myr}, \end{cases} \tag{5}$$

In our simulations, we find that the dynamical effect of this pressure does not depend on the numerical implementation of the steep decline. Note that the chosen value of the initial pressure is close to that measured in *evolved* H II regions. In this sense, it is the most conservative estimate of the dynamical effect of photoheating due to massive stars.

(3) Thermal energy from SNII is deposited in the cell containing a star particle of age less than 40 Myr at a constant rate $\Gamma' = 1.59 \times 10^{34}\,{\rm erg\,s^{-1}\,M_\odot}^{-1}$ obtained by modelling a simple stellar population using the stellar evolution code STARBURST99 for a Chabrier IMF. The energy is injected for a period of 40 Myr without artificially preventing gas cooling. The SNIa thermal energy injection rate is about 3 orders of magnitude lower than the rate for SNII. It peaks 1 Gyr after the formation of a star particle and declines over several billion years. Further details of the SN feedback employed here can be found in Ceverino & Klypin (2009).

Although the model described above is an extrapolation from sub-parsec scales to the tens-of-parsec scales resolved in our simulations, it incorporates several features that are fundamentally different from sub-grid feedback implementations. As mentioned above, the power contained in the radiation field is hundreds of times larger than in SN explosions and stellar winds. In addition, radiative forcing occurs as soon as the star cluster forms and drops rapidly once SNe begin to explode. Moreover, the model contains essentially no free parameters and is based on physical principles. The parameters that cannot be modelled are taken directly from observations. Thus, our implementation of stellar feedback is a step towards a physical rather than a phenomenological approach to forming galaxies in numerical simulations.

2.2 Star formation

To find a suitable model of SF, we again turn towards observations of SF in molecular clouds. Krumholz & Tan (2007) showed that at scales of 1–100 pc molecular clouds form stars at a rate that is proportional to the gas density divided by the free-fall time. For reasons that are yet not fully understood, this process is very slow, with only about 1–3 per cent of the gas consumed in one free- fall time in galactic molecular clouds. For the most active star-forming complexes in the MW – which are responsible for one third of the total SF – Murray (2011) find that the mass-weighted efficiency per free-fall time may be as high as 8 per cent. Since our simulations resolve regions a few times larger than the size of typical molecular clouds, we allow cold ($T < 1000$ K) gas to form stars once its density exceeds the value $n_{\rm SF} = 7\,{\rm cm^{-3}}$. At such densities, most gas in the simulation has very low temperatures around a few hundred Kelvin. Stars are formed at a rate

$$\frac{{\rm d}\rho_*}{{\rm d}t} = \epsilon_{\rm ff} \frac{\rho_{\rm gas}}{t_{\rm ff}}, \tag{6}$$

where $t_{\rm ff} \approx 5$ Myr is the typical free-fall time of observed molecular clouds, and $\epsilon_{\rm ff}$ is the observationally constrained efficiency per free-fall time. Following Ceverino & Klypin (2009), we include the effect of runaway stars. This is implemented by assigning to 33 per cent of the newly created stellar particles velocities sampled from a random

exponential distribution with a characteristic velocity of 17 km s^{-1} and random orientations.

2.2.1 *The impact of SF efficiency on feedback*

High-resolution simulations require a way to limit the number of star particles to relieve the computational burden of *N*-body calculations. This is typically done either by creating star particles stochastically with low probabilities or by limiting the minimum mass that a star particle may have. In most high-resolution simulations star particles are created by stochastically sampling equation (6) using $\epsilon_{\rm ff} \sim 1$–10 per cent (e.g. Stinson et al. 2006, 2010; Brooks et al. 2007; Governato et al. 2007, 2010, 2012; Ceverino & Klypin 2009; Guedes et al. 2011; Brook et al. 2012, 2014; Calura et al. 2012; Munshi et al. 2013; Ceverino et al. 2014; Christensen et al. 2014; Shen et al. 2014). By construction, this approach will produce individual SF events with large ratios of stellar mass to gas mass to compensate for the events where no stars are allowed to form. Only in the limit of high probability for each SF event, does this ratio approach the observed value, $M_{\rm star}/M_{\rm gas} = \epsilon_{\rm ff}\Delta t/t_{\rm ff}$, with $\epsilon_{\rm ff} \approx 1$–8 per cent. For instance, Christensen et al. (2014) adopt a model of SF in molecular hydrogen in their simulations but convert 33 per cent of the local gas mass into stars in each SF event. More recently, Brook et al. (2012) use a similar stochastic recipe, converting about 20 per cent of gas mass into star in each event. These numbers are a factor of ∼2–3 larger than the average observed efficiency of star clusters in the MW, $\epsilon_{\rm ff} \approx 8$ per cent (Murray 2011).

Although the typical $M_{\rm star}/M_{\rm gas}$ values of individual SF events in simulations are unrealistically high, they increase the strength of the stellar feedback and enhance gas blowouts from star-forming regions. Moreover, this artificial efficiency sometimes requires adjustment by a factor of 2 for haloes of different mass in order to obtain stellar masses that fall on the Moster et al. (2013) stellar-mass–halo-mass relation (Brook et al. 2012). Besides artificially inflating the local SF efficiency, the stochastic approach also inflates the stars-to-gas mass ratio, which in turn boosts the energy released by feedback. As a consequence, the energy release will be highly inhomogeneous and concentrated in a few high-efficiency regions. To avoid these issues in our model, we remove the lower mass limit for star particles and allow the mass to be controlled solely by the observed efficiency for *each* SF event, $\epsilon_{\rm ff}$.

Unfortunately, using deterministic SF in cosmological simulations is prohibitely expensive because the long gas consumption times yield particles with very small masses. The typical distribution of initial star particle masses in our runs has a narrow peak at ∼200 M$_\odot$, with 99 per cent of the particles in the range $50 < M/{\rm M}_\odot < 3000$. To avoid the computational cost of tracking large numbers of particles, we implemented a novel method for reducing the number of old stellar particles in the simulation. In this procedure, the mass contained in stars is resampled by periodically removing a small fraction (typically $\lesssim 10$ per cent) of old (age > 40 Myr) star particles while redistributing their total mass and metals uniformly among the remaining particles of the same age. This method preserves the total stellar mass of the galaxy while enforcing the observed *local* efficiency for each SF event. Appendix A compares the relation between surface density of SF and cold gas surface density obtained using our SF model with observations at kiloparsec scales.

In the following section, we estimate the effect of a local model of SF on the disruption of star-forming clouds. We show that the efficiency of SF is crucial in controlling the total energy and momentum output from young stars, which in turn determines whether the cloud expands and is dispersed by stellar feedback or collapses further to continue fuelling SF.

3 ANALYTICAL ESTIMATES OF THE EFFECTS OF STELLAR FEEDBACK

In this section, we provide analytical estimates of the effects of thermal and radiative feedback on the gas surrounding a young star cluster. We examine three conditions necessary for stellar feedback to have an effect on galaxy formation: (1) the overpressuring of gas due to SN heating, (2) the outward pressure from radiation, photoheating, SN and shocked stellar winds versus the confining pressure and (3) the fate of the gas once the cloud is dispersed.

3.1 Heating

For stellar feedback to be effective in dispersing the birth gas cloud, the outward gas pressure gradient must overcome self-gravity. In the case of SNe feedback, this is accomplished by injecting thermal energy to increase the gas temperature and pressure. For the cloud temperature to increase, the heating rate must be larger than the cooling rate of the gas due to radiative losses. The radiative cooling rate is $\Lambda = n_{\rm H}^2\Lambda'$, and the heating rate is $\Gamma = \rho_*\Gamma'$, where $n_{\rm H}$ and $\rho_\star$ are the number density of hydrogen atoms and the mass density of young stars, respectively. Using equation (6), we obtain the ratio of SNe heating to radiative cooling during one free-fall time:

$$\frac{\Gamma}{\Lambda} = \frac{\rho_*\Gamma'}{n_{\rm H}^2\Lambda'} = \frac{\epsilon_{\rm ff}}{n_{\rm H}}\left(\frac{\mu_{\rm H} m_{\rm H}\Gamma'}{\Lambda'}\right), \tag{7}$$

which depends only on the gas density and the SF efficiency. Fig. 2 shows the ratio of the heating rate to the cooling rate as a function of gas density for cold, solar metallicity gas. We take

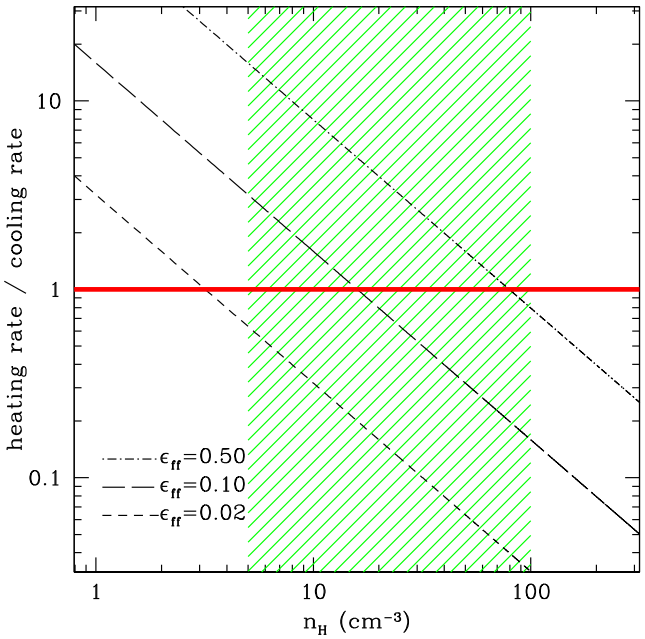

Figure 2. Ratio of heating rate due to SNII and shocked stellar winds to the cooling rate of cold gas as a function of gas density at $T \approx 100$ K for different values of the SF efficiency, $\epsilon_{\rm ff}$. The hatched area shows the typical range in SF density thresholds in high-resolution galaxy simulations. Only for values above the horizontal solid line is thermal feedback able to overpressure the gas before the energy is radiated away.

$\Gamma' = 1.59 \times 10^{34}\,\mathrm{erg\,s^{-1}\,M_\odot{}^{-1}}$ (which includes the contribution from shocked stellar winds), and assume that the gas is initially cold ($T \sim 100$ K), which gives $\Lambda' \approx 10^{-25}\,\mathrm{erg\,s^{-1}\,cm^3}$. Evidently, realistic values of $\epsilon_{\rm ff}$ overheat the gas *only* if SF occurs at densities below $\sim 3\,\mathrm{cm^{-3}}$. In typical high-resolution galaxy formation simulations, $n_{\rm SF} \gtrsim 1\,\mathrm{cm^{-3}}$, which implies that, for a free-fall time, the cooling rate will be larger than the heating rate and the gas will radiate its energy before it can expand.

3.2 Pressure gradient

Even if the temperature of the gas increases, stellar feedback will be ineffective unless it can pressurize the gas enough to overcome the force of gravity at the scales resolved in the simulation. Fig. 3 shows an estimate of the pressure in star-forming gas as a function of the cloud gas density compared to self-gravity and the external pressure of the ISM. The pressure due to self-gravity is $P_{\rm grav} = 4\pi G \rho_{\rm gas} R^2/3$, where R is the radius of the cloud. The pressure of the ISM is assumed to be $P_{\rm ISM}/k_{\rm B} = 5 \times 10^3\,\mathrm{K\,cm^{-3}}$, RP is calculated using equation (4), and the thermal pressure due to photoheating is set to $P_{\rm PH} = 2 \times 10^6\,\mathrm{K\,cm^{-3}}$. In the comparison, we show the effect of increasing the local efficiency of SF and the optical depth of the gas using two cases. Assuming $\epsilon_{\rm ff} = 5$ per cent and $\tau_{\rm tot} = 5$, at densities $3 \lesssim n_{\rm H} \lesssim 100\,\mathrm{cm^{-3}}$, where SNe heating cannot exceed radiative cooling, stellar radiation overpressures the gas by a factor of up to $\sim$10 (for $\tau_{\rm tot} \leq 5$) with respect the inward

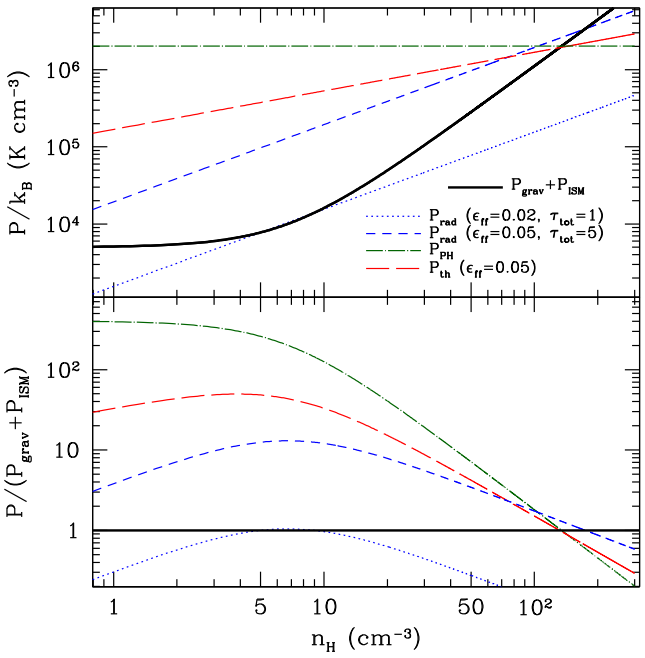

Figure 3. Different contributions to the gas pressure inside a star-forming region using a realistic local SF model. Top: comparison of 'blastwave' pressure, stellar RP and the inward pressure due to self-gravity and the ambient medium at the typical resolution of our simulations ($\Delta x = 50$ pc). Bottom: ratio of the outward to the inward pressure. 'Blastwave' pressure is calculated assuming that the gas cooling is delayed as is commonly done is simulations, and that the energy injection stops after one dynamical time. For RP, the curves show the effects of different assumptions about the local SF efficiency and the gas optical depth. At the gas densities resolved in our simulations ($n_{\rm H} \lesssim 10\,\mathrm{cm^{-3}}$), photoheating dominates over the other mechanisms, while radiation momentum overpressures gas by a factor of 1–10 for $\tau_{\rm tot} \leq 5$. The 'blastwave' pressure is $\sim$50 times greater than the inward pressure.

pressure from self-gravity and the ambient medium. This outward pressure gradient will cause the expansion of a low-density cavity around the star cluster and halting of subsequent SF. Fig. 3 also shows an estimate of the pressure resulting from injection of SNII thermal energy and artificially delayed gas cooling (as in the widely used 'blastwave' approximation; Stinson et al. 2006). Since in this method cooling is typically delayed for a several million years, we calculate the thermal gas pressure that results from the increase in internal energy during a free-fall time, $P_{\rm th} = M_* \Gamma' t_{\rm ff}/(\Delta x)^3$, where M_* is the total mass of massive stars and Δx is the size of the grid cell. Initially, the large continuous energy injection rapidly increases the temperature and pressure of the gas, reaching $T \gtrsim 4 \times 10^8$ K in the first million years after the formation of the massive stars. At these temperatures the sound speed is several hundred kilometres per second and the sound crossing time is about $\sim$1000 times smaller than the dynamical time. Before the system can adjust, the pressure inside the region reaches values $\sim$5 times larger than the RP and about 50 times the inward pressure. This large gradient causes the region to expand explosively, creating the gas blowouts that are ubiquitous in simulations that use 'blastwave' SNe feedback. Once the gas density drops, the pressure gradient vanishes. In contrast, RP remains at a constant value of several times the self-gravity, allowing for a lower but continuous evacuation of the gas from star-forming regions. Moreover, in contrast to SNe feedback, RP does not heat the gas to millions of degrees in order to disperse the star-forming cloud.

3.3 Gas escape

Once the overpressured gas is able to overcome self-gravity and expand, its fate depends on the amount of momentum it acquires from feedback. The baryon fraction, the SFR and the metallicity of the galaxy will depend critically on whether gas ejected from star-forming regions falls back on to the galaxy or is able to escape the galactic potential without ever returning. Fig. 4 shows the ballistic velocity of the gas surrounding a stellar cluster as a function of time as a result of radiation feedback *only* (with no SNe or stellar winds), as implemented in Section 2, for different values of the SF efficiency, $\epsilon_{\rm ff}$. To obtain the velocity, we integrate the equation of motion using the total force exerted on the gas inside a cell by radiation, self-gravity and the ISM, $F_{\rm tot} = (P_{\rm rad} + P_{\rm PH} - P_{\rm grav} - P_{\rm ISM})(\Delta x)^2$. Fig. 4 shows that single scattering of radiation alone accelerates gas beyond the typical escape velocities of low-mass galaxies ($\gtrsim$100 km s^{-1}) only for high SF efficiencies, $\epsilon_{\rm ff} \gtrsim 30$ per cent. For realistic values of the efficiency, $\epsilon_{\rm ff} \approx$ 1–8 per cent, either large infrared dust optical depths ($\tau_{\rm IR} \gtrsim 30$) or photoheating are necessary to eject gas from the galaxy at velocities exceeding the escape velocity. The fate of the gas subject to stellar feedback will have important implications to the fraction of baryons that stay within the galaxy and its circumgalactic gas.

4 NUMERICAL SIMULATIONS

In this paper, we analyse the formation of galaxies within two DM haloes which bracket a broad range within the mass spectrum of low-mass galaxies. One is representative of a dwarf galaxy with a mass $M_{\rm vir} = 3 \times 10^{10}\,\mathrm{M_\odot}$, and the second one is about 10 times more massive and is comparable to a typical field spiral galaxy with $M_{\rm vir} = 2 \times 10^{11}\,\mathrm{M_\odot}$. The galaxies formed within these two haloes are designated 'dwarf' and 'spiral', respectively, throughout the paper. To investigate the stellar mass assembly in these DM haloes, we performed numerical simulations with a variety of different stellar

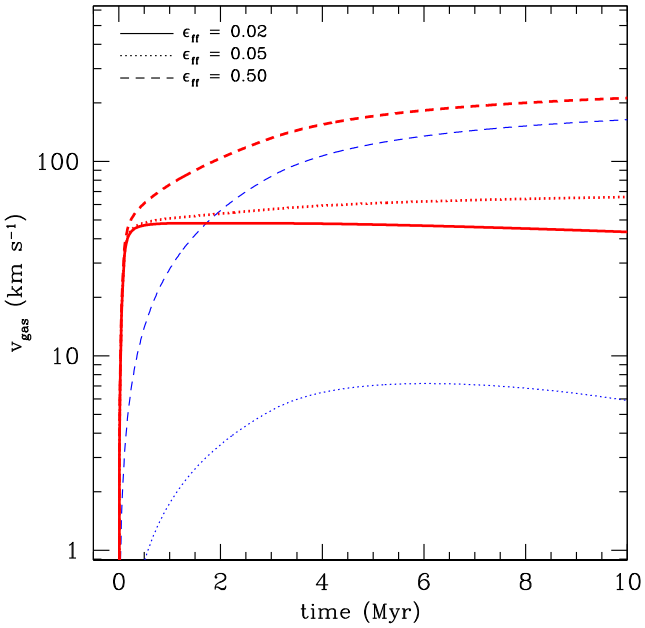

Figure 4. Gas velocity as a result of radiation feedback from an embedded star cluster. We assume that the only forces acting against the expansion are the self-gravity of the gas cloud and the confining pressure of the surrounding ISM. Solid, dotted and dashed lines correspond to different values of the SF efficiency, $\epsilon_{\rm ff}$, assuming an optical depth of the gas $\tau_{\rm tot} = 1$. Thin curves show RP only, while thick curves include RP and photoheating. For realistic local SF efficiencies (i.e. $\epsilon_{\rm ff} = 0.01$–0.08), radiation momentum does not accelerate gas beyond the typical escape velocity of a low-mass galaxy. Gas escapes the galactic potential only when photoheating is included or the infrared optical depth is large.

feedback prescriptions. All the simulations used the cosmological parameters $\Omega_{\rm m} = 1 - \Omega_\Lambda = 0.30$, $\Omega_{\rm b} = 0.045$, $\sigma_8 = 0.8$ and $h = H_0/(100\,{\rm km\ s^{-1}\,Mpc^{-1}}) = 0.7$. Each simulation 'zooms-in' on a single isolated DM halo inside a $10\,{\rm h^{-1}Mpc}$ comoving box, achieving a maximum resolution of 40–80 h^{-1} pc at $z = 0$. Throughout the paper, we define virial mass as the total mass (baryonic and DM) enclosed within a spherical region with an average density equal to the virial overdensity in the top-hat collapse model, $\Delta_{\rm vir}$, times the average density of the Universe at that redshift. Table 1 summarizes the general properties of the DM haloes used in this work.

All the simulations in this paper use a deterministic model of SF where stars from in cold and dense gas with $n > 7\,{\rm cm^{-3}}$ and $T < 1000\,{\rm K}$. The gas density threshold is chosen to be smaller than the density at which the gas is artificially pressurized to prevent spurious fragmentation (Truelove et al. 1997). This paper focuses on the differences between feedback models that include only standard SNe thermal feedback versus models with radiation feedback. We dedicate most of the following discussion to a model with only thermal feedback (`SN` runs) and a fiducial radiative feedback model

Table 1. Properties of the DM-only simulations at $z = 0$.

Halo	$M_{\rm vir}$ ($M_\odot$)	$R_{\rm vir}$ (kpc)	Minimumc ell size (pc h^{-1})	DM mass resolution ($M_\odot$)
`dwarf`	3×10^{10}	80	40	9.4×10^4
`spiral`	2×10^{11}	150	80	7.5×10^5

which includes the effect of single scattering of radiation and photoheating from ionization (`ALL_1` and `ALL_8`). Table 2 shows the parameters of the feedback prescriptions used in each simulation. In addition, we test the effect of variations in the parameters of radiation feedback as explained below.

4.1 Duration of radiative forcing

In addition to the models discussed above, we tested the effect of varying the duration of radiative forcing on the gas around each star particle in the simulations. In the real birth clouds of stellar clusters the radiation is initially trapped by the high column density of the gas surrounding the cluster. This forcing vanishes once the gas column density decreases enough to become optically thin to UV/optical photons.

Our simulations do not resolve the physical column densities involved in star-forming regions, so we must estimate the time when RP becomes negligible. To do this, we set a density threshold below which the extra pressure is switched off in the cells adjacent to the star particle. We tested several models of radiative feedback using two different thresholds: $n_{\rm th} = 0.1\,{\rm cm^{-3}}$ and $n_{\rm th} = 0.01\,{\rm cm^{-3}}$. Lower threshold values result in a longer duration of radiative forcing up to a maximum of 40 Myr (in the `_long` models).

4.2 Infrared trapping of radiation

In addition to the duration of radiative forcing, there is uncertainty in the optical depth of the gas to the reprocessed IR photons, $\tau_{\rm IR}$. As discussed above, observations and simulations using radiative transfer favour values between as high as ∼50 (Agertz et al. 2013; Davis et al. 2014) for young clusters. In two simulations of the `dwarf` halo, we investigate varying the infrared optical depth within the range preferred by models and observations, setting $\tau_{\rm IR} = 10$ and $\tau_{\rm IR} = 50$.

4.3 Thermal pressure due to photoheating

As discussed in Section 2.1, there is substantial variation in the thermal pressure of gas in observed H II regions, with about an order of magnitude scatter between individual regions. Furthermore, the photoheating pressure must have been larger than that of evolved regions at the early stages of evolution, when densities were higher. To account for this uncertainties, we test a range of values of the pressure, $P_{\rm PH,\,0} = 10^6 - 4 \times 10^7\,{\rm K\,cm^{-3}}$ in our numerical experiments. We refer to models in which the photoheating pressure is varied but the RP is fixed using the `ALL_#` label, where the number denotes the multiplier of the fiducial value, $10^6\,{\rm K\,cm^{-3}}$.

5 RESULTS

5.1 Global properties and galaxy formation efficiency

Table 3 shows the integrated properties of the simulated galaxies. Stellar and gas masses are computed within 10 kpc from the galaxy centre. We define the baryon fraction, $f_{\rm bar}$, as the ratio of the total baryonic mass within 10 kpc to the virial mass. Table 3 shows that for the `dwarf` as well as for the `spiral` galaxies, the stellar mass and the ratio of gas to stellar mass, $M_{\rm gas}/M_*$, change drastically when RP and photoheating feedback are included. Models with only SNe feedback suffer from catastrophic overcooling, which results in excessive SF and a conversion of a large fraction of halo baryons into stars. The stellar mass of the `dwSN` model is more than six

Table 2. Parameters for feedback and SF in the simulations. SNII+SW indicates SNe and stellar winds, RP stands for radiation pressure and PH denotes photoheating.

Model	$\epsilon_{\rm ff}$	Feedback	$\tau_{\rm tot}$	$P_{\rm PH}/k_{\rm B}$ (10^6 K cm^{-3})	$n_{\rm th}$ (cm^{-3})
dwSN	0.02	SNII+SW	–	0	–
dwRP_1_long	0.05	SNII+SW+RP	1	0	0.01
dwRP_10_long	0.05	SNII+SW+RP	10	0	0.01
dwRP_50_long	0.05	SNII+SW+RP	50	0	0.01
dwALL_1	0.05	SNII+SW+RP+PH	1	1	0.1
dwALL_8	0.02	SNII+SW+RP+PH	1	8	0.1
dwALL_40	0.02	SNII+SW+RP+PH	1	40	0.1
dwALL_8_long	0.02	SNII+SW+RP+PH	1	8	0.01
spSN	0.02	SNII+SW	–	–	–
spALL_8	0.02	SNII+SW+RP+PH	1	8	0.1
spALL_40	0.02	SNII+SW+RP+PH	1	40	0.1
spALL_8_long	0.02	SNII+SW+RP+PH	1	8	0.01

Table 3. Global galaxy properties.

Model	Redshift	$M_{\rm vir}$ ($M_\odot$)	M_* ($M_\odot$)	$M_{\rm gas}$ ($M_\odot$)	$M_{\rm gas,\,cold}$ ($M_\odot$)	$M_*/M_{\rm vir}$	$M_{\rm gas,\,cold}/M_*$	$f_{\rm bar}$
dwSN	0	3.0×10^{10}	8.1×10^{8}	8.1×10^{8}	5.5×10^{8}	2.7×10^{-2}	0.7	0.054
dwALL_1	0	3.2×10^{10}	1.3×10^{8}	2.1×10^{9}	1.4×10^{9}	4.1×10^{-3}	10.8	0.070
dwALL_8	0	2.8×10^{10}	2.1×10^{7}	5.5×10^{8}	1.2×10^{8}	7.5×10^{-4}	5.7	0.020
dwALL_40	0	2.7×10^{10}	7.5×10^{6}	1.9×10^{8}	1.3×10^{7}	2.8×10^{-4}	1.7	0.007
dwALL_8_long	0	2.9×10^{10}	1.6×10^{7}	7.4×10^{8}	6.2×10^{7}	5.5×10^{-4}	3.9	0.026
spSN	2.3	8.3×10^{10}	1.4×10^{9}	3.7×10^{9}	2.1×10^{9}	1.7×10^{-2}	1.5	0.061
spALL_8	1.3	1.9×10^{11}	6.4×10^{8}	1.0×10^{10}	7.6×10^{9}	3.4×10^{-3}	11.9	0.056
spALL_40	1.3	1.7×10^{11}	7.9×10^{7}	4.0×10^{9}	2.2×10^{9}	4.7×10^{-4}	27.8	0.024
spALL_8_long	1.3	1.9×10^{11}	4.9×10^{8}	8.9×10^{9}	6.5×10^{9}	2.6×10^{-3}	13.3	0.049

times greater than the fiducial radiation feedback model dwALL_1, even though dwALL_1 has a 2.5 times greater efficiency of SF, $\epsilon_{\rm ff}$. While not shown, simulations with RP but no photoheating also have large stellar masses at $z > 1$ (see Fig. 7) showing that radiation momentum alone (with $\tau_{\rm IR} \leq 50$) is not sufficient to reduce the total stellar mass in low-mass haloes. In the low-mass spiral, the failure of standard SN feedback is more serious due to the deeper potential well. At $z \approx 2.5$, the spSN simulation has more than 50 times the stellar mass of the spALL_8 model.

All the models with radiation feedback produce galaxies with stellar-to-halo mass ratios that are in good agreement with the semi-empirical models of Behroozi et al. (2013) and others (Firmani & Avila-Reese 2010; Moster et al. 2013). For instance, using DM-only cosmological simulations and constraints from observations at many redshifts, Behroozi et al. (2013) obtain a ratio $M_*/M_{\rm vir} \sim 0.0025$ for a halo of mass $M_{\rm vir} = 3 \times 10^{10}\,M_\odot$ at $z = 0$. Among the dwarf simulations, the fiducial model with RP and photoheating (dwALL_1) shows the best agreement with this value, falling within its 1σ systematic uncertainty. This comparison is shown in Fig. 5, where we also include estimates from other probes such as weak lensing (Miller et al. 2014), and mass-modelling (Oh et al. 2011b). Models with stronger radiative coupling ($10 < \tau_{\rm tot} < 50$) generally have similar stellar masses. Once photoheating is included, additional tests show that it becomes the main driver of the decrease in the stellar mass of the ALL models. Dwarf simulations with increased photoheating pressure fall below the 1σ distribution in Behroozi et al. (2013) but fit comfortably inside other estimates such as those by Moster et al. (2013) and Oh et al. (2011b). However, since different observational inferences predict discrepant stellar-to-virial mass ratios, it is difficult to rule out models based on this diagnostic alone.

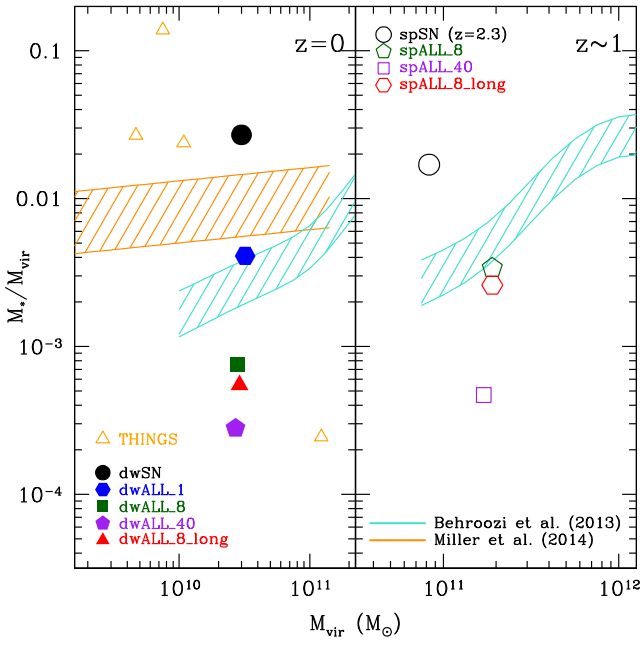

Figure 5. Stellar-to-virial mass ratio of the simulated galaxies. Left: dwarf models at $z = 0$. Right: spiral models at $z \approx 1$. For comparison, the hatched areas show the 1σ systematic envelope of the semi-empirical model by Behroozi et al. (2013), as well as the Miller et al. (2014) inference from observations, and individual mass models from Oh et al. (2011b). While SNe energy alone (dwSN) leads to overproduction of stars compared to Behroozi et al., including stellar radiative feedback reduces the stellar mass drastically. Note that the effect of RP is robust to large variations in the parameters $\tau_{\rm tot}$ and $n_{\rm th}$ (modulo changes in the SF efficiency parameter, $\epsilon_{\rm ff}$).

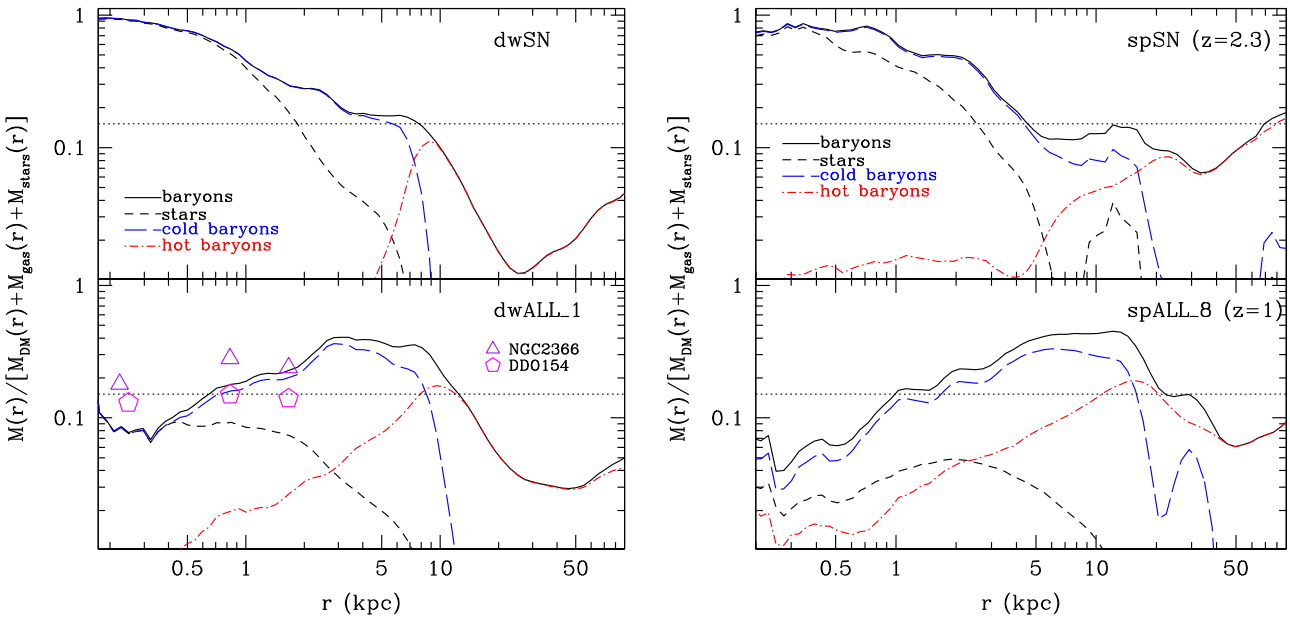

Figure 6. Baryon mass fraction radial profiles. The curves show the ratio of the mass in each baryonic component to the total mass as a function of radius, $M_{\rm bar}(r)/M_{\rm tot}(r)$. 'Cold baryons' include stars and gas with $T < 10^4$ K, whereas 'hot baryons' represents gas with $T > 10^4$ K. The dotted horizontal line represents the universal baryon fraction. Left: `dwarf` models. Open symbols show the estimated $M_{\rm bar}/M_{\rm tot}$ in the central regions of two isolated dwarf irregular galaxies from the THINGS survey (Oh et al. 2011a). Right: `spiral` models. SNe energy cannot prevent the accumulation of cold baryons in the inner ∼2 kpc. Stellar RP and photoheating reduce the mass of baryons in the galaxy by heating and expelling cold gas out into the CGM.

The cumulative effect of radiative feedback at $z = 0$ is not highly sensitive to variations in the parameters within the uncertainties in the physical model. For $M_{\rm vir} = 3 \times 10^{10}$ M$_\odot$, a factor of 5 increase in forcing and a factor of ∼10 change in duration of the effect produce a variation no larger than a factor of ∼3 in the stellar mass for simulations with the same $\epsilon_{\rm ff}$ (compare the `ALL_8`, `ALL_8_long` and `ALL_40` models).

Table 3 lists the ratio of cold gas mass to stellar mass within 10 kpc of the centre of each galaxy. We define cold gas as gas with $T < 10^4$ K. The cold gas fractions of galaxies with SN feedback are smaller than unity, showing that a large amount of the cold and dense gas that is available to form stars is quickly consumed. On the other hand, models with RP have gas fractions as large as ∼30, which indicates that the galaxies are inefficient at converting their gas into stars. Observations of cold atomic and molecular gas in galaxies at $z = 0$ reveal an anticorrelation between stellar mass and gas fraction, with galaxies of mass $M_* = 1 \times 10^8$ M$_\odot$ containing $M_{\rm gas,cold}/M_* \sim 4.7^{+5.3}_{-2.5}$, decreasing to ∼1.6 for $M_* = 1 \times 10^9$ M$_\odot$ (Dutton et al. 2011). Thus, our dwarf galaxies with radiative feedback display excellent agreement with observations, showing that radiation from massive stars plays a key role in maintaining large cold gas reservoirs in low-mass galaxies.

One essential characteristic of low-mass galaxies that simulations still struggle to reproduce is their extremely low galaxy formation efficiency, or in other words, the amount of primordial baryons that condense to form the galaxy. For a galaxy with the mass of the MW, semi-empirical models based on matching the abundance of galaxies to that of DM haloes (e.g. Behroozi et al. 2010, 2013; Trujillo-Gomez et al. 2011; Moster et al. 2013) predict an efficiency $M_*/M_{\rm vir} \sim 25$ per cent, whereas for a dwarf galaxy with $M_* = 10^8$ M$_\odot$ the ratio is an order of magnitude smaller, $M_*/M_{\rm vir} \sim 2.5$ per cent. The last column of Table 3 shows the baryon fraction, $f_{\rm bar} \equiv [M_*(<10\,{\rm kpc}) + M_{\rm gas}(<10\,{\rm kpc})]/M_{\rm vir}$ for all the model galaxies.

In general, stellar radiation does not seem to have a large effect on the baryon fraction of low-mass DM haloes. For both the `dwarf` and the `spiral` simulations, the total baryon fraction within the virial radius and within the galaxy are virtually unaffected by radiation feedback. Focusing on the dwarf simulations, we find that the total baryon fraction within the galaxy ($r < 5$ kpc) is ∼25 per cent, and is ∼5 per cent within the virial radius when only SN feedback is included. In models with RP and photoheating, the baryon fraction is relatively unchanged at ∼25 per cent within the `dwALL_1` galaxy and ∼7 per cent within its virial radius. Surprisingly, this implies that the amount of baryons retained within the halo is not affected by feedback due to radiation from massive stars.

To investigate the physical origin of this feature, we plot in Fig. 6 the ratio of the mass in each baryonic component to the total mass as function of radius from the centre of the galaxy, $M_{\rm bar}(r)/M_{\rm tot}(r)$. We include the baryons locked in stars, as well as the cold and hot baryons. 'Cold baryons' include stars and gas with $T < 10^4$ K, and 'hot baryons' correspond to gas above 10^4 K. It is evident in the figure that although the baryon fractions do not change significantly when radiation feedback is included (see Table 3), the inner part of the galaxies is modified drastically. In the `SN` simulations, cold baryons contribute 50–90 per cent of the total mass in the central regions of the galaxy ($r < 2$ kpc in the `dwSN` and $r < 5$ kpc in the `spSN` model), which is up to six times larger than the universal fraction of baryons. Furthermore, the central baryons in these galaxies are dominated by stars. In contrast, the simulations with radiative feedback are dominated by DM at all radii. The central contribution of stars to the mass in these models is never greater than 8 per cent in `dwALL_1` and no larger than 6 per cent in `spALL_8`. However, cold gas contributes a larger fraction of the total baryon mass between ∼1 and 10 kpc. This reduces the average ratio $M_{\rm bar}(r)/M_{\rm tot}(r)$ to a value near 15 per cent, or about the cosmic mean.

In conclusion, when accounting for the baryon budget within the galaxy and within the circum-galactic medium (CGM), we

highlight three main consequences of stellar radiation. First, as discussed above, the total fraction of mass in baryons within the central ∼1–3 kpc, where most of the SF takes place, is reduced to values near the cosmic mean, and even below the cosmic mean for smaller radii. Secondly, the amount of cold gas at intermediate distances, $1 \lesssim r \lesssim 10$ kpc, is much larger when radiation feedback is included, comprising about 30 per cent of the total mass at 10 kpc. Thirdly, the fraction of mass in gas with $T > 10^4$ K increases dramatically within the `dwarf` and `spiral` galaxies due to RP and photoheating enhancing the effect of SNe feedback. Together, these features indicate that the main role of radiation from massive stars is to control the amount of gas that is converted to stars within the galaxy by dispersing and heating it, and ejecting some into the halo, where it can remain in a warm, dilute phase. We note that there is also an increased amount of cold gas in the CGM of the fiducial RP simulations. In a forthcoming paper (Trujillo-Gomez et al., in preparation) we analyse the properties of gas in the context of accretion and outflows.

5.1.1 Discussion

Our results show that including radiation feedback from young massive stars reduces the stellar mass growth in dwarf and low-mass spiral galaxies. Taken at face value, detailed comparisons with abundance matching models seem to indicate that the combination of momentum from radiation and ionization photoheating are sufficient to prevent excessive SF in haloes with $M_{\rm vir} \sim 3 \times 10^{10} - 2 \times 10^{11}$ M$_\odot$ enough to bring them into agreement with observations.

From detailed observations of the structure of nearby dwarf irregulars (dIrrs) we can perform case-by-case comparisons. Oh et al. (2011a) obtained mass models of dIrrs using multiwavelength data. Their models constrained the 'cold baryon' mass fraction $M_{\rm bar}/M_{\rm tot}$ within the optical extent of galaxies with $V_{\rm max} \approx 50$–60 km s^{-1} to values ∼15–35 per cent. Our results show that SN feedback is unable to prevent the build-up of stars in the central few kiloparsecs, which leads to large baryon fractions within the galaxy. In contrast, the fiducial radiation feedback model, with single photon scattering, reduces the mass of baryons that is locked in stars within the galaxy to values near the cosmic mean, in very good agreement with Oh et al. (2011a). In addition, a distinctive feature of the simulation with radiation feedback is that cold gas dominates the baryon budget within 10 kpc (see Fig. 6), with a ratio of cold gas mass to stellar mass that is in excellent agreement with observations (see Section 5.1).

In general, the trend we find among the variations of the radiation feedback model is that a larger photoheating pressure or longer duration of radiative forcing reduces the baryon fraction further than in the fiducial model. However, both the total baryon fraction and the stellar baryon fraction within the virial radius are quite robust to the large variations in the choice of feedback and SF parameters. Among the models with RP and photoheating, with the optical depth varying by a factor of 40, and $\epsilon_{\rm ff}$ varying by a factor of 2.5, the baryonic and stellar mass fractions vary by less than a factor of ∼3.

It is important to note that the term 'baryon fraction' has a variety of definitions in the literature. Usually, in observations, it corresponds to the ratio of the mass of a galaxy in neutral atomic gas, molecular gas and stars within its optical extent to the estimated total gravitational mass out to the virial radius. In our runs with full feedback (the `ALL` models), cold gas dominates the baryons within the galaxy, contributing ∼20 per cent of the total mass within 10 kpc, whereas within the virial radius most baryons are in the form of warm/hot gas with $T > 10^4$ K. Following this definition, in the fiducial full radiation feedback models the 'observed' baryon fraction is ∼4–5 per cent, about 40 per cent smaller than the total baryon fraction. As shown in Fig. 6, this is *not* due to escape of baryons from the halo, but instead it relates to an increase in the mass of warm/hot gas at $10 < r < 70$ kpc. Pressure from stellar radiation and photoheating is thus sufficient to match the observed 'cold baryon' content of low-mass galaxies estimated from observations without the need for ad hoc winds that cause the escape of large amounts of gas from the halo. These results agree with the conclusions of a companion paper, Ceverino et al. (2014), where it is shown that massive galaxies ($M_{\rm vir}(z = 0) \approx 10^{12}$ M$_\odot$) at high redshift require RP to reduce the fraction of baryons in stars to the low values obtained in constrained abundance matching models (e.g. Behroozi et al. 2013).

Other simulation works have recently reported success in reproducing the observed galaxy formation efficiency as a function of mass (e.g. Brook et al. 2012; Haas et al. 2013; Munshi et al. 2013; Vogelsberger et al. 2013). Vogelsberger et al. (2013) compute the stellar-to-halo mass fraction in large volume hydrodynamic simulations that use phenomenological SF and galactic wind prescriptions. They obtain values that are consistent with ours and with abundance matching constraints. We emphasize that for galaxies with $3 \times 10^{10} < M_{\rm vir}/{\rm M}_\odot < 2 \times 10^{11}$, radiative feedback fully accounts for the observed stellar-to-halo mass ratios without expelling a majority of the baryons from the halo, but instead by regulating SF and keeping most of the gas at low densities in the CGM (see Fig. 6).

5.2 Stellar mass assembly and star formation history

In this section, we present the stellar mass assembly histories of the simulated galaxies. Fig. 7 compares the stellar mass as a function of time for all the models. The stellar mass assembly rate of all the dwarf galaxies with full radiative feedback is nearly constant in time with a tendency towards faster growth at late epochs ($z < 1$) for models with smaller photoheating values. In contrast, the models with only SN feedback show a period of extremely fast growth in the initial ∼3 Gyr, where most of the stellar mass is formed, followed by very slow growth thereafter. Including only SN energy and radiation momentum with low IR optical depth results in a small reduction of the stellar mass at high redshift followed by rapid growth at $z \sim 1$. The figure indicates that the large reduction in the present-day stellar content of models with full radiative feedback versus models with only SNe energy results from a reduced SFR since the time of the onset of SF until $z = 0$. Furthermore, photoheating pressure from young clusters is the main driver of the large suppression of growth at early times ($z > 2$), when the galaxies with SN feedback and radiation momentum grow rapidly due to the large gas accretion rates at high redshift. A combination of these two effects, the drop in the SFR at all epochs and the reduction of the early runaway SF, result in dwarf galaxies that assemble a large fraction (∼50 per cent) of their stars late ($z < 1$), in agreement with the observed phenomenon of galaxy 'downsizing' (e.g. Baldry et al. 2004; Noeske et al. 2007; Whitaker et al. 2012). The more massive `spiral` model with stellar RP and photoheating behaves similarly to the dwarf galaxies, with a highly suppressed stellar mass growth at early times, continuing as far as the simulations have been run.

The bottom panels of Fig. 7 show the virial mass of the galaxy as a function of time. The stellar mass of the SN simulations closely

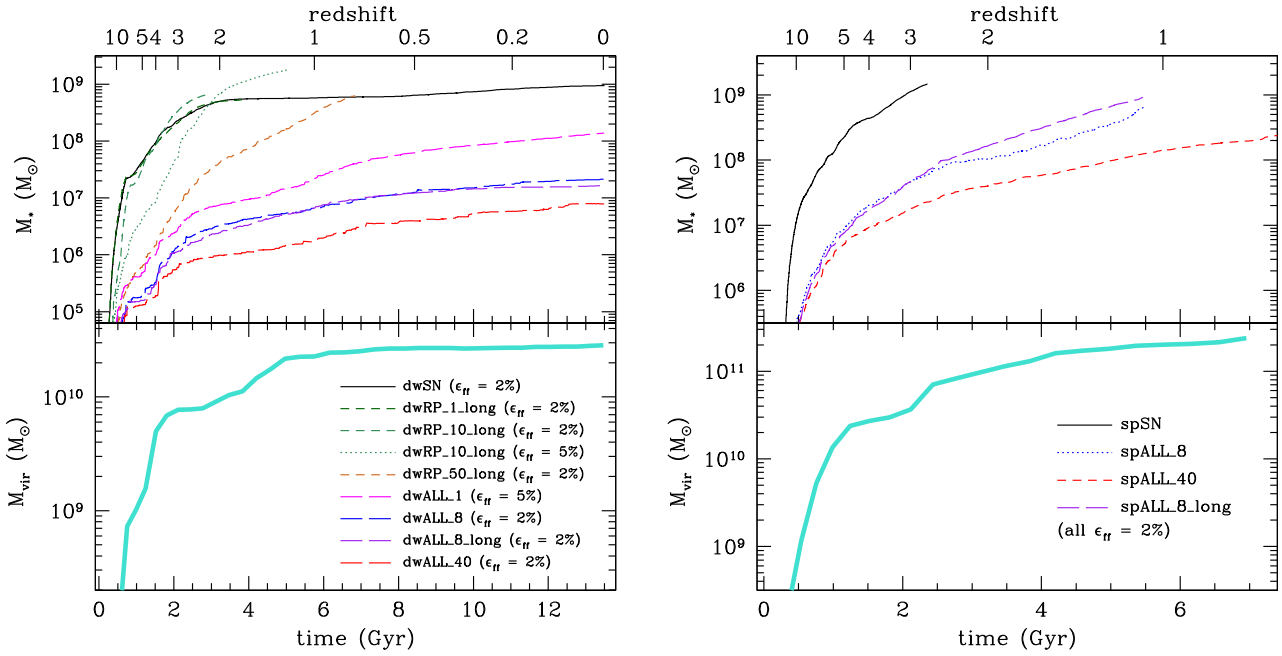

Figure 7. Stellar and virial mass as a function of time. Left: `dwarf` models. Right: `spiral` models. Radiation momentum alone only delays the growth of stellar mass at early times. However, low-mass galaxy models that include stellar RP and photoheating show a dramatic reduction in the stellar mass growth at all epochs compared to a model with only SNe feedback. Moreover, only galaxies that include the effect of photoheating tend to build up more than half of their stellar component after $z = 1$, displaying nearly constant SFR in agreement with observations of Local Group dIrrs. The stellar mass growth of galaxies with radiative feedback is rather insensitive to large variations in the model parameters.

follows the rate of assembly of the DM, both in the overall shape and in the individual episodes of fast growth due to mergers. In contrast, during the epoch of fast growth of the virial mass, stellar radiation is able to delay the conversion of newly accreted gas into stars, decoupling the growth of the galaxy from the growth of the DM halo. Moreover, radiative feedback also delays the episodes of stellar mass growth due to mergers by ∼1–2 Gyr relative to the growth of the total mass.

As discussed in Section 1, most high-resolution galaxy formation simulations to date which are able to reproduce the properties of present-day galaxies suffer from the overproduction of stars at high redshift. This problem is especially pronounced for MW-mass haloes and less severe in dwarf galaxy simulations. Our `spiral` halo is a prime candidate to test the growth rate of the stellar component at high redshift against observations. The top-right panel of Fig. 9 shows the semi-empirical star formation histories (SFHs) from Behroozi et al. (2013) for a typical galaxy with a present-day virial mass $M_{\rm vir} = 10^{11}\,{\rm M}_{\odot}$, along with the 1σ scatter. The agreement with our simulations including radiative feedback is remarkable, given that there is no fine-tuning of the parameters. The slightly larger SFR in the simulations is not significant since our galaxy has a virial mass two times larger than the Behroozi et al. value, so its SFR is expected to be a few times larger. Hence, radiative feedback from young stars seems to be an essential ingredient in regulating the growth of low-mass galaxies at early times. It is important to note that there is remarkable agreement among the models with radiative feedback. Fig. 7 indicates that the assembly histories of models with $\epsilon_{\rm ff} = 2$ per cent differ at most by a factor of ∼3. This is much smaller than the variation in the strength of the radiative forcing among the models. The main driver of the higher SFR in `dwRP_1` is the larger local SF efficiency. In the more massive galaxy the variations are larger possibly due to the deeper potential well. In general, the variations due to the assumed optical depth of the gas and dust are much smaller than the differences that result from the new physics of stellar radiative feedback.

The top-left panel of Fig. 9 shows the SFHs of the models calculated in 1 Gyr time bins to approximate the typical time resolution in observations. The dwarf model with standard SNe feedback has very large SFR at early times when gas accretion rates are high, but the SFR gradually decreases by a factor of ∼30–100 at later epochs. In contrast, SFR in dwarfs that include stellar RP and photoheating are suppressed by a factor of ∼100–500 at $5 < z < 2$, and stay nearly constant or sometimes increase towards the present. The situation is similar in the `spiral` models, where radiative feedback reduces the early SFR by a factor of ∼100–200 at $z \approx 4$. These reduced early SFR in isolated dwarfs are in excellent agreement with resolved stellar population studies of nearby dIrrs (Weisz et al. 2011a,b) as well as with extrapolations of abundance matching models. The observed delay in the SF at $z > 1$ in low-mass galaxies may be caused by radiation ejecting and dispersing cold star-forming gas out of the galaxy and into the halo, where dilute gas is stored in a reservoir that condenses back on to the galaxy after a few billion years ($z < 1$) to fuel the late period of SF. In Section 5.6, we show that the radial distribution of gas supports this conclusion.

On the bottom-left panel of Fig. 9, we plot the 'burstiness' of the SFHs. This is quantified by taking the ratio between the SFR calculated in narrow, 20 Myr bins and the SFR calculated in broad, 1 Gyr bins. All the dwarfs with full radiative feedback show large bursts that are comparable in frequency, with typical episodes where the SFR doubles occurring every few hundred million years, and the largest bursts increasing the SFR by a factor of ∼5–10. All the simulations with SNe feedback have much smoother SFHs with less pronounced and less frequent bursts. The broad SFR peaks in this model likely correspond to major mergers (since we do not distinguish here between in situ and ex-situ SF). For the higher mass `spiral` models, the bottom panel of Fig. 9 shows that in all

the runs with radiative feedback the amplitude and frequency of star bursts are similar and less intense than in the dwarf galaxy analogue runs, reaching about 2–3 times the SFR averaged over 1 Gyr bins.

5.2.1 *Discussion*

SFHs that peak at high redshift are ubiquitous not only in simulations of massive galaxies (e.g. Governato et al. 2007; Agertz, Teyssier & Moore 2011; Calura et al. 2012; Scannapieco et al. 2012), but they also seem to be generic in dwarf galaxy simulations. In a simulation of a galaxy with $M_{\rm vir} \sim 2 \times 10^{11}\,{\rm M}_\odot$, and a feedback model tuned to match present-day galaxies, Governato et al. (2007) obtain a star formation history that peaks at $z \sim 1$ and declines by a factor of 2 by $z = 0$. Their physical model does not include RP. Instead, they increase the effect of thermal SN feedback by delaying gas cooling in star-forming regions using the 'blastwave' model (Stinson et al. 2006). In more recent work, Christensen et al. (2014) present SPH simulations of the formation of dwarf galaxies of mass $\sim 10^{10}\,{\rm M}_\odot$, which is close to the virial mass of our dwarf halo. Even after including SF in molecular hydrogen (which reduces the SF efficiency in low metallicity gas), the SFR reaches a maximum in the first ~6–8 Gyr of cosmic time, with a slow decline of a factor of ~2 thereafter. Using a similar feedback prescription, Brook et al. (2011) simulate the formation of a dwarf galaxy and obtain an SFR that peaks at $z \sim 1$ and quickly declines by a factor of 10 at low redshift. In recent work, Brook et al. (2012) performed SPH simulations of low-mass galaxies that try to mimic the effect of RP by boosting the SNe energy yield to unrealistic values. Their dwarf galaxies show SFHs that are nearly constant. However, their halo with $M_* \sim 10^{11}\,{\rm M}_\odot$ overproduces stars at $z > 1$, with SFR $\sim 0.5\,{\rm M}_\odot\,{\rm yr}^{-1}$ at $z = 2$, a factor of ~10 larger than the prediction by Behroozi et al. (2013), and SFR $\sim 0.1\,{\rm M}_\odot\,{\rm yr}^{-1}$ at $z = 3$, a factor of ~5 larger than in Behroozi et al. (2013). Thus, increasing the efficiency of SN feedback to unrealistically high values does not seem to reduce the early SFR sufficiently to reproduce the effect of radiative feedback and the observed growth of low-mass galaxies.

Resolved stellar population studies of Local Group as well as isolated dIrrs (Weisz et al. 2011a,b) show that their average sSFRs are constant in time within the uncertainties. Table 4 shows both the SFR and the sSFR of selected dwarf simulations averaged over the last Gyr to mimic the time resolution of the youngest populations in Weisz et al. (2011a). Weisz et al. (2011a) determine an average present-day sSFR $\approx 1 \times 10^{-10}\,{\rm yr}^{-1}$ for a sample of 43 dIrrs, which is in excellent agreement with the sSFRs of our fiducial dwarf model with full radiative feedback (`dwALL_1`; see Table 4).

In particular, for NGC 2366, which resembles `dwALL_1` in stellar mass and circular velocity (see Section 5.3), Weisz et al. (2011a) find a present-day SFR $\approx 4 \times 10^{-2}\,{\rm M}_\odot\,{\rm yr}^{-1}$, also in excellent agreement with the value of $2.6 \times 10^{-2}\,{\rm M}_\odot\,{\rm yr}^{-1}$ that we obtain for this run.

Table 4. SFR for selected runs. Values are averaged over 1 Gyr.

Model	z	SFR(z) (${\rm M}_\odot\,{\rm yr}^{-1}$)	sSFR(z) (${\rm yr}^{-1}$)
`dwSN`	0	5.3×10^{-2}	6.5×10^{-11}
`dwALL_1`	0	2.6×10^{-2}	2.0×10^{-10}
`dwALL_8`	0	1.7×10^{-3}	7.9×10^{-11}
`dwALL_40`	0	9.9×10^{-4}	1.3×10^{-10}
`dwALL_8_long`	0	1.3×10^{-3}	7.9×10^{-11}
`spSN`	3.0	5.6	1.9×10^{-9}
`spALL_8`	1.3	8.9×10^{-1}	1.4×10^{-9}
`spALL_40`	1.3	9.6×10^{-2}	1.2×10^{-9}
`spALL_8_long`	1.3	9.3×10^{-1}	1.9×10^{-9}

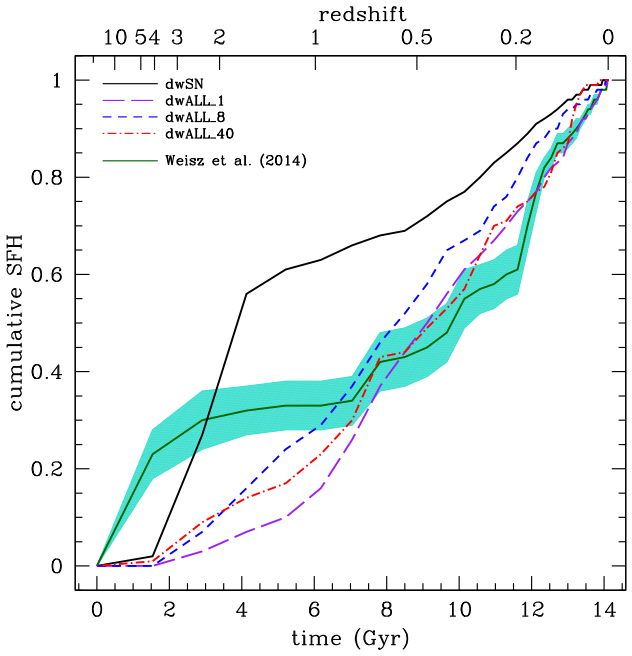

Figure 8. Cumulative SFH of `dwarf` runs compared to Local Group dIrrs. The data corresponds to the stellar mass formed prior to a given time averaged across all the dIrrs in the Weisz et al. (2014) sample. The shaded area shows the standard error in the mean. Only the simulations with RP and photoheating reproduce the stellar mass growth st $z < 1$. The statistical uncertainties in the observed data (not shown) are larger at $z > 1$.

The sSFR at $z = 0$ in our fiducial dwarf galaxy with stellar radiation feedback is $\sim 0.2\,{\rm Gyr}^{-1}$, an order of magnitude larger than the value reported by Governato et al. (2010) for `DG1`, a simulation tuned to produce a realistic isolated dwarf galaxy with a mass $M_{\rm vir} = 3.5 \times 10^{10}\,{\rm M}_\odot$. Salim et al. (2007) show that the average sSFRs of low-mass star-forming galaxies measured using UV light and nebular emission lines are well fitted by the relation ${\rm sSFR} = -0.35(\log M_* - 10.0) - 9.83$ at $z \approx 0$. For a galaxy with the stellar mass of `dwALL_1`, this relation gives an average ${\rm sSFR} = 6.8^{+14.7}_{-4.6} \times 10^{-10}\,{\rm yr}^{-1}$, where the error bars indicate the intrinsic scatter in the galaxy population. Averaged over the last billion years, the sSFR of `dwALL_1` is $2 \times 10^{-10}\,{\rm yr}^{-1}$, in excellent agreement with the observations by Salim et al. (2007). For comparison, the sSFR in the `dwSN` simulation is about a factor of 3 smaller. In the simulations of the higher mass halo with RP and photoheating, the sSFR at $z \sim 1$ is 1.2–1.9 $\times 10^{-9}\,{\rm yr}^{-1}$, which is in excellent agreement with the $z = 1$ measurements by Dunne et al. (2009) and Gilbank et al. (2011), adjusted to a Chabrier IMF as shown in Avila-Reese et al. (2011). Stellar radiation, with photoheating playing the dominant role, is then essential in regulating early SF and maintaining a large supply of gas to sustain a high SFR at $z < 1$. This process may also cause the decoupling of the growth of the DM halo from the growth of the stellar component of low-mass galaxies at high redshift.

Weisz et al. (2014) assembled the most complete set of *Hubble Space Telescope* observations of Local Group dwarfs and performed a uniform analysis of the SFHs. They find that dIrrs only formed about 30 per cent of their stars by $z = 1$. Fig. 8 shows our results compared to the average cumulative SFHs of the irregulars from Weisz et al. (2014). Clearly, SN energy alone results in larger than

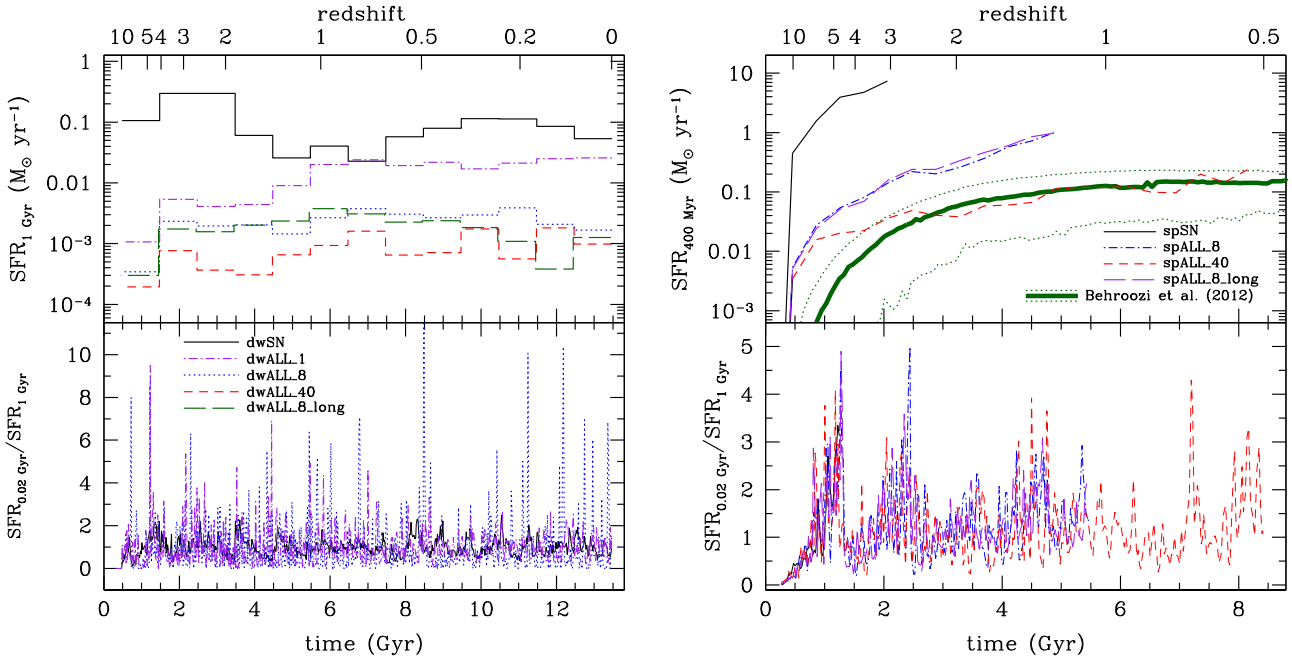

Figure 9. SFHs. Left: `dwarf` models. Right: `spiral` models. The top panels show the SFHs in broad bins, while the bottom panels show the amplitude of the bursts in 20 Myr bins relative to the smooth histories. The dwarf galaxy with only SN energy forms stars aggressively in the initial ∼3 Gyr and its SFR slowly decreases thereafter. This also occurs when only RP is added if the IR optical depth is small (not shown). In contrast, including both RP and photoheating reduces the early SFR by a factor of $\gtrsim$100, while the galaxies are able to maintain a constant or even increasing rate of SF until $z \sim 0$, in agreement with observations of dIrrs. Simulations with radiation feedback have burstier SFHs than models with only SNe, especially for $z < 1$. The top-right panel compares the SFH of `spiral` models with a semi-empirical result for a galaxy with $M_{\rm vir} = 10^{11}\,{\rm M}_{\odot}$ (solid curve with the 1σ scatter represented by dotted lines), showing very good agreement only when full stellar radiation feedback is included.

observed stellar masses throughout the history of the galaxy. The simulations with full radiation feedback reproduce the observed SFH at $z < 1$, where the systematic uncertainties in the data are the smallest. As deeper and more complete data becomes available, the abundance of the oldest stars in dwarf galaxies should place better constraints on the role of feedback in small haloes at early epochs (e.g. Madau, Weisz & Conroy 2014).

Current observations do not reach the time resolution necessary to measure the burstiness of individual galaxies. However, Weisz et al. (2012) fit simple models to observations and determine that galaxies with $M_* < 10^7\,{\rm M}_{\odot}$ have bursty SFHs with amplitude ratios ∼30, while more massive dwarfs are consistent with smooth SFHs. The bottom panel of Fig. 9 shows the same qualitative behaviour in our models. There is a trend of increase in burstiness in the SFHs for galaxies with stronger radiative forcing or lower stellar mass. Furthermore, the model with only SN feedback has the smoothest SFH. In sharp contrast, dwarfs with both RP and photoheating feature frequent bursts with amplitude ratios as large as ∼5–10 when measured in 20 Myr bins.

5.3 Mass distribution

In this section, we analyse the detailed radial distribution of each mass component of the simulated galaxies. We use the circular velocity, which is a proxy for mass, and is defined as $v_{\rm circ} = \sqrt{GM(<r)/r}$.

Fig. 10 presents the circular velocity curves of simulations with standard SN feedback versus models including full radiation feedback. The figure also shows the contributions from each component, including DM, stars and gas. Both models with only SNe feedback, `dwSN` and `spSN`, display a strong signature of overcooling in circular velocity curves that are sharply peaked in the central ∼1 kpc and quickly decrease at larger radii. In contrast to observed rotation curves of low-mass galaxies, these models are dynamically dominated by stars within the inner ∼1–2 kpc. This occurs due to the excessive growth of a concentrated stellar component in the central region of the galaxy. In all the models with full radiative feedback the galaxies are dominated by DM within ∼10 kpc and the contribution of baryons to the mass is small at small radii. Both haloes with radiative feedback also have a reduced stellar component at all radii compared to models with only SN energy. The difference is more pronounced within the central 2 kpc, where gas is able to collapse and form stars actively unless feedback can disperse it. Fig. 10 demonstrates that in galaxies with $3 \times 10^{10} < M_{\rm vir}/\,{\rm M}_{\odot} < 2 \times 10^{11}$ RP and photoheating not only reduce the total stellar mass of the galaxy, but they preferentially prevent excessive SF in the central kiloparsec by dispersing and blowing out the cold and dense gas that continuously flows in. Among the simulations with radiative feedback, the mass distribution is quite robust to large changes in the parameters of the radiation feedback implementation, $\tau_{\rm tot}$ and $n_{\rm th}$. In all cases, the galaxies have slowly rising, DM-dominated circular velocity profiles where gas contributes most of the baryons at all radii.

Circular velocity profiles allow for direct comparisons with observed rotation curves of low-mass galaxies at $z = 0$. The THINGS survey (Oh et al. 2011a) presented detailed observations of dwarf irregular galaxy rotation curves from H I observations. Using ancillary infrared *Spitzer* data, they were able to decompose the mass distribution of gas-rich dwarfs. In general, these detailed models show that dwarf galaxy rotation curves are slowly rising and dominated by DM at any distance. In Table 5, we directly compare our fiducial dwarf galaxy with full radiative feedback with two

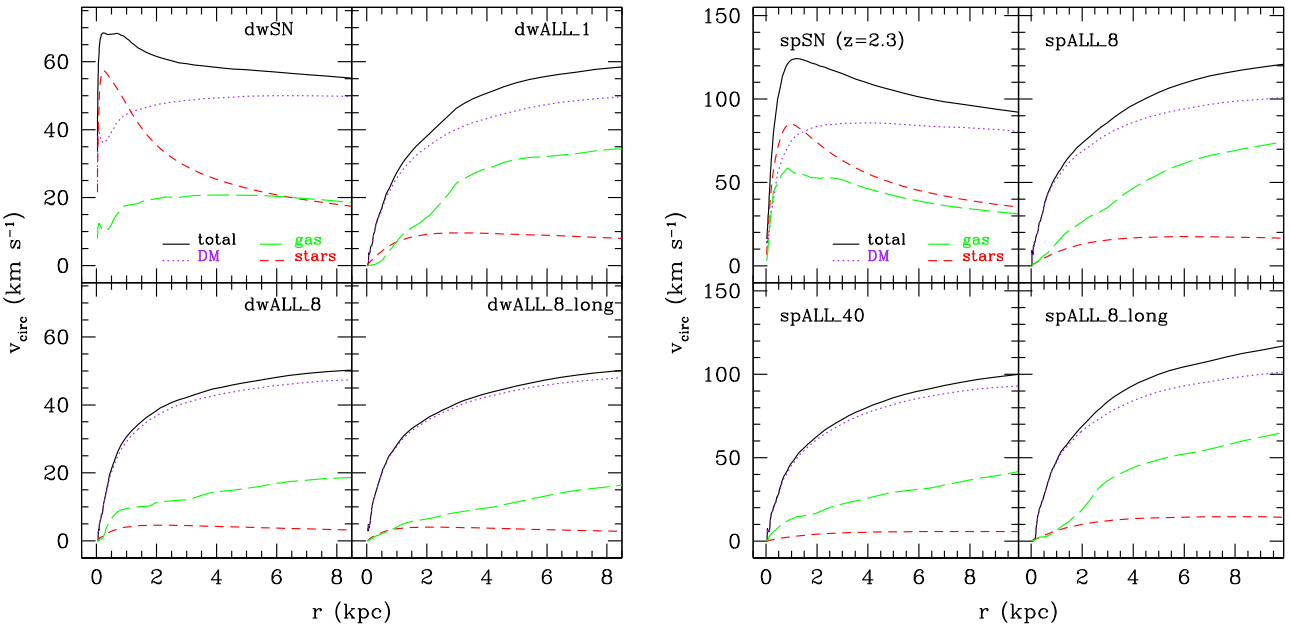

Figure 10. Circular velocity profiles. The solid curve shows the total, the dotted line shows the DM and the long and short dashed lines show the gas and stars, respectively. Left: `dwarf` models at $z = 0$. Right: `spiral` models at $z \approx 1$–2. The mass distribution in models with only SN energy is dominated by a massive stellar component in the central 1–2 kpc. Radiative feedback ejects and dilutes star-forming gas and prevents the formation of a concentrated stellar component. There is remarkable agreement in the mass distribution of models with full radiative feedback. All produce slowly rising, DM-dominated profiles with most of the baryons in the gas phase.

Table 5. Circular velocity profile of the fiducial dwarf simulation with radiative feedback compared to two observed dIrrs from Oh et al. (2011a).

Radius (kpc)	$v_{\rm circ}(r)$(km s^{-1})		
	`dwALL_1`	NGC 2366	DDO154
1.0	25	22	27
2.0	40	33	38
4.0	55	43	52
8.0	65	50	58

galaxies from Oh et al. (2011a), NGC 2366 and DDO154, which have similar maximum circular velocities to our models.

The circular velocity profile of the fiducial model with full stellar radiation feedback is a very good match to rotation curves of observed galaxies of similar mass, NGC 2366 and DDO154, except perhaps in the central ∼1 kpc, where the rise in the circular velocity of the fiducial run is slightly steeper. In addition, Oh et al. (2011a) determine maximum circular velocities for the stars and cold gas in NGC 2366 of ∼15 km s^{-1} and 28 km s^{-1}, respectively. For DDO154 they find maximum values $v_{\rm circ} \sim 7$ km s^{-1} for the stars, and $v_{\rm circ} \sim 20$ km s^{-1} for neutral atomic hydrogen. Our fiducial model with radiative feedback has a maximum stellar $v_{\rm circ} \sim 10$ km s^{-1}, and $v_{\rm circ} \sim 35$ km s^{-1} for gas at any temperature.

5.4 Do baryons influence the DM distribution?

There has been a debate in the literature over the past 20 years about the steepness of the inner DM density profile of galaxies. The 'cusp-core problem' originates from the standard prediction of CDM models that the density of DM should increase steeply (as $r^{-\alpha}$, with $\alpha \sim 1$) towards the centre of the halo at the smallest scales that can be probed by simulations (Flores & Primack 1994; Moore 1994). Ever since this prediction was made, observations have attempted to robustly obtain the density profile of the DM in the inner kiloparsec of disc galaxies using detailed mass modelling (e.g. de Blok & McGaugh 1997; de Blok et al. 2001; Blais-Ouellette et al. 2004; Rhee et al. 2004; Simon et al. 2005; Oh et al. 2008; Kuzio de Naray, McGaugh & Mihos 2009; Adams et al. 2012). Some works obtain very shallow, constant-density 'cores', while others find steep 'cusps' consistent with CDM. Even though great effort has gone into reducing the systematics, observations using different mass tracers still yield conflicting results. Most recently, Oh et al. (2011a) studied a sample of dIrrs using H I as a tracer and consistently obtained shallow DM slopes, $\alpha \approx 0.3$. On the other hand, using both stellar and nebular gas kinematics, Adams et al. (2014) obtain a variety of steeper slope values for different galaxies, covering the range ∼0.5–0.8.

Several mechanisms have been proposed to explain the observed shallow slopes. While most require revisions of the CDM model, one relies purely on baryonic effects. This scenario involves the 'heating' of the DM due to feedback processes. Analytical models and simulations with strong SNe 'blastwave' feedback have recently shown that gas blowouts in low-mass galaxies have the potential to alter the distribution of DM in the central regions. Mashchenko, Wadsley & Couchman (2008), Pontzen & Governato (2012), Governato et al. (2012) and Teyssier et al. (2013) argue that large and frequent bursts of SF which cause gas blowouts and a rapid oscillation in the potential should transform an initially cuspy DM distribution into a shallow core. However, those simulations are different from the ones presented here in two respects. First, none of these works include radiative feedback from massive stars, and secondly, the SFHs of simulated dwarf galaxies that include SN feedback with delayed cooling usually peak at $z > 1$, whereas the SFR of the simulations presented here peaks at $z < 1$ (see Section 5.2). In fully cosmological simulations the core is already in

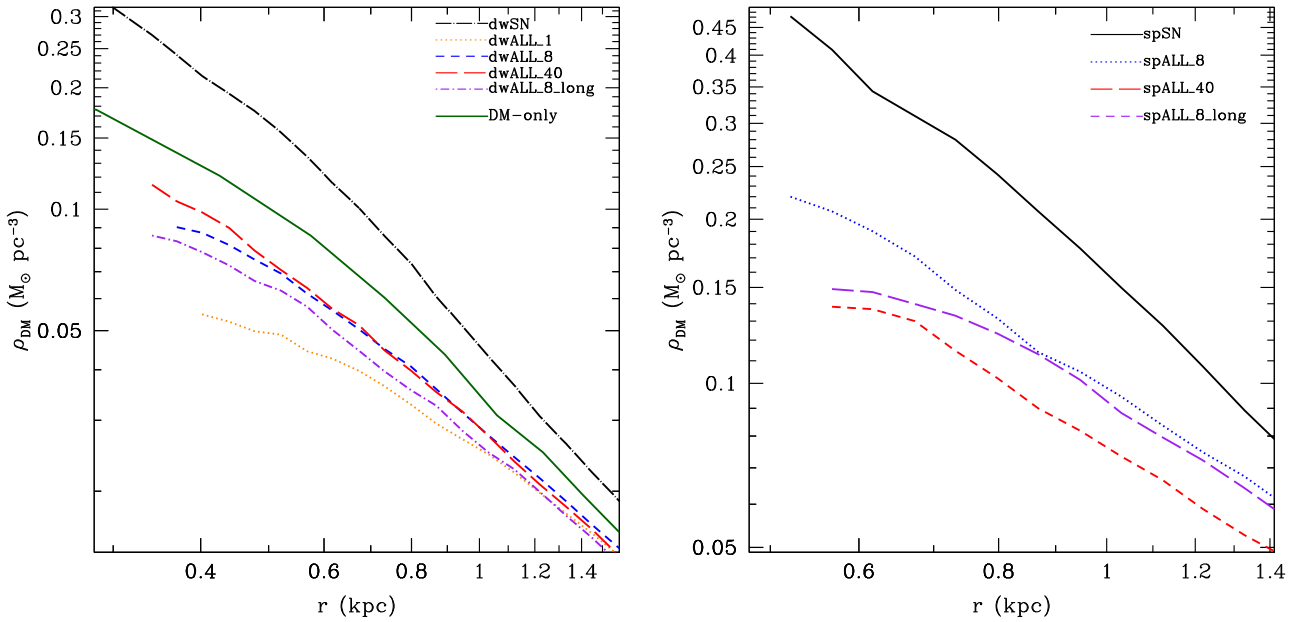

Figure 11. Inner DM density profiles. Left: `dwarf` models at $z = 0$. The solid line shows the profile of the same simulation run without baryons. Right: `spiral` models at $z \approx 1$–2. The central DM mass distribution in models with only SN explosions is contracted due to the presence of a concentrated massive stellar spheroid, resulting in a steep cusp. RP and photoheating from massive stars creates a shallow DM core within ∼1 kpc in the `dwALL_1` run as well as in spiral-size haloes with greater photoheating pressure or longer radiative forcing (`spALL_40` and `spALL_8_long`).

place at $z \approx 3$ (Governato et al. 2012; Pontzen & Governato 2012) or even earlier (Mashchenko et al. 2008), so this raises the question of how the mass distribution of the galaxy will respond to radiative feedback and its effect of reducing the SFR a high redshift.

The top panels of Fig. 11 show the inner DM density profiles of the simulations. Several models with full radiative feedback are included to investigate any differences that might arise from the details of the feedback implementation. In addition, for the lower mass halo, we include the profile of the same DM halo simulated without baryons. The profiles are truncated at the radius enclosing ∼200 DM particles to avoid numerical artefacts due to resolution in the inner regions (Klypin et al. 2013). Clearly, Fig. 11 shows that in our runs with only SNe feedback, the early runaway SF in the central kiloparsec increases the central DM density compared to the run without baryons. This causes an increase of a factor of ∼2 in the DM density at 700 pc and a factor of ∼3 at 400 pc. Halo contraction has been studied in depth in analytical works as well as simulations (Blumenthal et al. 1986; Gnedin et al. 2004, 2011; Duffy et al. 2010; Tissera et al. 2010). It results from baryons in the central regions of the halo dragging the surrounding DM into a more concentrated equilibrium configuration. In sharp contrast with the SN run, the simulations with full radiative feedback show shallower density profiles. However, measuring the slope of the density profile reveals that only the fiducial RP and photoheating model, `dwALL_1`, has a slope that is shallower than -1 at $r \geq 500$ pc. A different behaviour is observed in the galaxies with $M_{\rm vir} = 2 \times 10^{11}$ M$_\odot$, where only the simulations with larger photoheating pressure ($P_{\rm PH}/k_B \gtrsim 4 \times 10^7$ K cm^{-3}) or longer duration of radiative forcing are able to reduce the DM density within 700 pc considerably by $z \sim 1$. This may be a consequence of the smaller relative amplitude of the SF bursts or the deeper potential well compared to the dwarf simulations (see Fig. 9).

Table 6 shows the logarithmic slope of the DM density profile, $\alpha \equiv \frac{{\rm d}\log\rho}{{\rm d}\log r}$. The inner slopes of simulations with radiation feedback are similar to the DM-only run, except in the case of the `dwALL_1` model, where the slope is significantly shallower. We find that as the photoheating pressure is increased, the slopes become progressively steeper and approach or exceed the slope of the run without baryons. Governato et al. (2012) suggest that the central DM density slope of simulated dwarf galaxies becomes steeper with decreasing stellar mass. Table 6 also shows the slopes of the DM profile at $300 < r < 700$ pc calculated using the Governato et al. (2012) relation for the stellar masses of each of our models. In general, stellar radiation feedback yields galaxies with steeper central slopes than the Governato et al. (2012) models with effective SNe blowouts. Moreover, our results are in stark contrast with the effects of the 'early feedback' model used by Brook et al. (2012). Injecting large amounts of SN thermal energy in star-forming regions, they obtain nearly flat DM inner density profiles with more than order of magnitude lower density than the DM-only runs for galaxies with

Table 6. Central DM profile slope of the simulations compared to the fit by Governato et al. (2012) and to the mass models of two observed dIrrs from Oh et al. (2011a). The slope in the simulations was obtained by fitting a power law to the spherically averaged density profile at $300 < r < 700$ pc. In the observations, the slope corresponds to a fit for $r < 1$ kpc.

Galaxy	α	$\alpha_{\rm G12}$
`dwALL_1`	−0.59	−0.46
`dwALL_8`	−1.10	−0.73
`dwALL_40`	−1.45	−0.89
`dwALL_8_long`	−0.84	−0.78
`dwDM`	−1.14	–
DDO154	-0.29 ± 0.15	–
NGC 2366	-0.32 ± 0.10	–

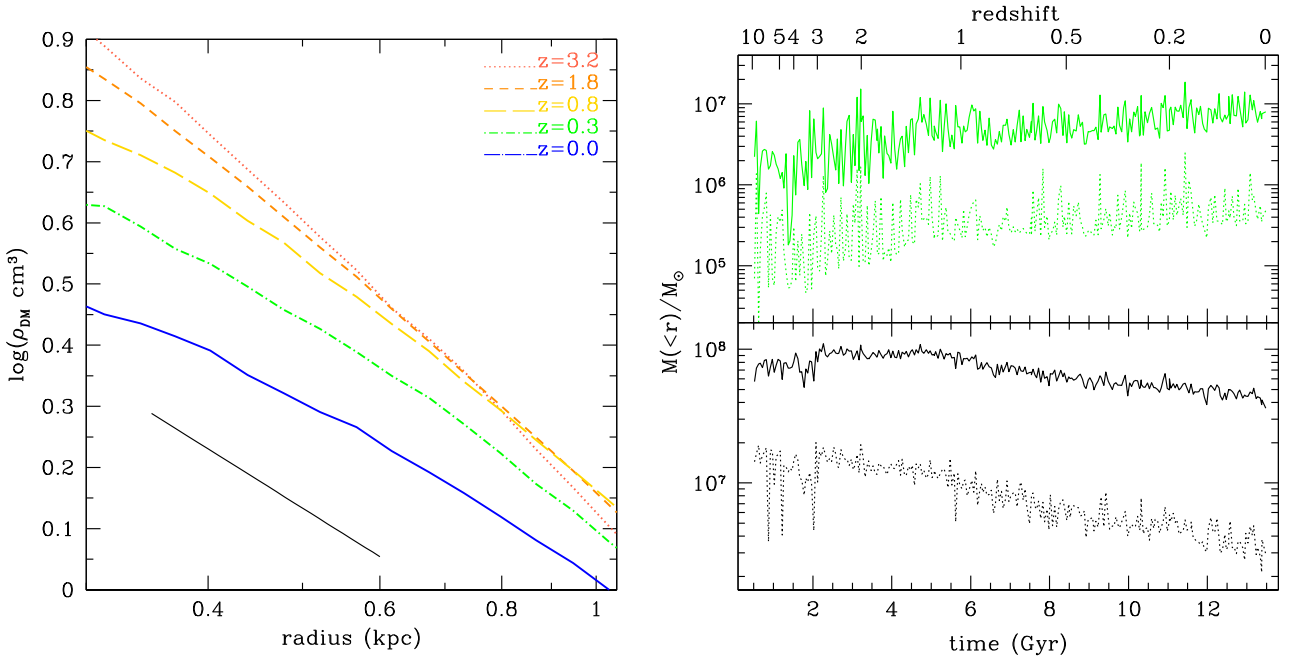

Figure 12. Evolution of the inner mass profile of the fiducial dwarf simulation with RP and photoheating, `dwALL_1`. Left: evolution of the DM density profile. The straight line corresponds to $\alpha = -1.0$. Note that the slope at high redshift is steeper than -1. Top right: baryonic mass (gas + stars) contained in the inner 500 (solid line) and 200 pc (dotted line) calculated every 50 Myr. Bottom right: same for total mass (baryons + DM). The central DM density decreases significantly after $z = 0.8$. Even though there are order-of-magnitude variations in the baryonic mass at early times, the dynamical mass only changes by a factor of ∼2–3.

$M_* < 4 \times 10^9\,\mathrm{M}_\odot$. Using a controlled simulation of a $10^{10}\,\mathrm{M}_\odot$ dwarf galaxy using thermal SNe feedback and delayed gas cooling, Teyssier et al. (2013) find that SF bursts with peak-to-trough ratios ∼5–10 are necessary to produce the gas blowouts that cause the formation of a shallow DM core. Our dwarf simulations with RP and photoheating undergo bursts that typically reach amplitudes ∼3–5 relative to the mean SFR (see Fig. 9). Hence, even though our radiative feedback is very effective at regulating the assembly of the stellar mass, our models have steeper DM profiles than simulations with extremely efficient SN feedback.

To compare our simulations directly with observations, Table 6 shows the slope of a power-law fit to the density profile between 300 and 700 pc in our main runs. The table also includes values from mass-modelling of two dIrrs from the THINGS survey, DDO154 and NGC 2366, obtained using H I and 3.6 μ observations (Oh et al. 2011a). These galaxies were chosen because their $v_{\rm max}$ is close to our dwarf simulations. In the observations, the slope was obtained from a fit to the profile within 1 kpc. Even though the fiducial model with radiative feedback, `dwALL_1`, has the shallowest profile, it is considerably steeper than observed dIrrs of the same mass. Note, however, that the logarithmic slope contains only partial information about the density profile. A comparison of the actual central density is more meaningful and less sensitive to noise. For instance, the DM density of NGC 2366 at a distance of 500 pc is $\rho_{\rm DM} \approx 0.04\,\mathrm{M}_\odot\,\mathrm{pc}^{-3}$, while for DDO154 the density at the same radius is $\approx 0.05\,\mathrm{M}_\odot\,\mathrm{pc}^{-3}$. The only simulated dwarf galaxy that shows a shallow profile, `dwALL_1`, has a central density $\rho_{\rm DM} = 0.052\,\mathrm{M}_\odot\,\mathrm{pc}^{-3}$ in excellent agreement with these values.

Fig. 12 shows the evolution of the inner DM density profile of `dwALL_1` since $z \sim 3$. There is a fast decrease of the density in the inner kiloparsec after $z \sim 1$, indicating that the DM 'core' begins to form at $z \sim 1$ and slowly grows over ∼7 Gyr. By $z = 0$ the density 400 pc from the centre has decreased by more than a factor of 2 compared to the density at $z > 2$. Only after $z = 0.2$ does the logarithmic slope of the density profile become shallower than -1. The right-hand panel of Fig. 12 also illustrates the evolution of the mass enclosed within the inner regions of the galaxy as a proxy for the time dependence of the gravitational potential. Even though there are large fluctuations in the baryonic mass within the inner kiloparsec, the dynamical mass changes by less than 50 per cent on small time-scales.

Pontzen & Governato (2012) discussed the origin of the shallow DM density profile in a simulation of a dwarf with a stellar mass $M_* = 3.7 \times 10^{10}\,\mathrm{M}_\odot$. At $z = 4$ the baryons in the simulation are dominated by gas, and large SNe blowouts cause fluctuations in the central gas mass ($r \lesssim 0.5$ kpc) of nearly an order of magnitude on time-scales shorter than the dynamical time of the galaxy. Our fiducial model with radiative feedback shows changes in the baryonic mass of comparable amplitude at high redshift, and decreasing thereafter. However, as shown on the left-hand panel of Fig. 12, the simulation does not form a 'core' for another several billion years, at $z \lesssim 0.3$. The right-hand panels of Fig. 12 show the time evolution of the central mass of the simulation. There are large variations in the central mass at early times. The dynamical mass, which drives the potential, shows fluctuations of only a factor of $\lesssim 2$ occurring preferentially during the second half of cosmic history. This behaviour is a result of the way that SF proceeds when radiation feedback is included. Since the SFR is very low at early times, and the central part of the DM halo is already in place, feedback is insufficient to produce large gas outflows. At lower redshift, the SFR rapidly increases by about an order of magnitude and drives increasingly more feedback energy and momentum into the galactic gas. This results in larger blowouts and stronger fluctuations of the central mass on short time-scales which eventually reduce the DM density

at late times. If, as observations suggest, galaxies of the same mass show a variety of DM central slopes, mergers might play a role in determining which ones evolve the steepest profiles.

5.5 The effect of radiation on galaxy morphology

Another observational constraint that is particularly difficult to reproduce in simulations is the thickness of the stellar distribution. State-of-the-art SPH simulations with 'blastwave' SNe feedback have recently produced disc-dominated galaxies with small bulge-to-total ratios in MW-mass haloes (e.g. Guedes et al. 2011; Brook et al. 2012). However, about 50 per cent of observed star-forming galaxies with $M_* = 10^{10}\,\mathrm{M}_\odot$ are bulgeless, and this fraction increases at lower luminosities (Dutton 2009). No simulation to date has been able to form a bulgeless galaxy of the same mass as the MW. For low-mass galaxies this crisis worsens. Blue galaxies with r-band luminosities $M_r > -18$ are essentially all bulgeless discs (Blanton et al. 2003). The situation changes for dwarf galaxies ($M_* < 10^9\,\mathrm{M}_\odot$) in the field, for which Geha et al. (2012) find that essentially all galaxies have blue colours and ongoing SF. These isolated dwarfs have irregular and patchy H I and UV morphologies with thick stellar distributions and axis ratios $b/a \lesssim 0.5$ (Mateo 1998; McConnachie 2012). In summary, the morphology of field galaxies provides very tight constraints for numerical models. Simulations of isolated dwarfs which include all the relevant physics should *always* produce blue, dispersion-dominated star-forming galaxies. On the other hand, simulated field galaxies with $M_{\rm vir} \sim 10^{11}\,\mathrm{M}_\odot$ should be thin, bulgeless discs. In this section, we analyse the stellar distribution of the stars in our models and compare them to observations of nearby galaxies.

Fig. 13 shows the distribution of the angular momentum of the star particles in the `dwarf` simulations. For each particle, the angular momentum is normalized to the angular momentum of a circular orbit at the same radius, $\epsilon \equiv j_z/j_c$. In these distributions, a rotation-dominated galaxy will show a large peak near $\epsilon = 1$, whereas a dispersion supported component would be dominated by stars with $\epsilon < 1$. With only SN feedback, the stars in the dwarf have circularities that peak at $\epsilon \approx 0.9$, with about 18 per cent of the stellar mass in circular orbits ($0.9 < \epsilon < 1.1$). In the fiducial model with radiative feedback (`dwALL_1`), the peak shifts towards lower values, $\epsilon \approx 0.5$, and the overall distribution of orbital circularity is broader, indicating that the galaxy is less supported by rotation than `dwSN`. The number of stars in nearly circular orbits decreases by ∼50 per cent with RP and photoheating. In addition, the distribution broadens as the photoheating pressure is increased and the peak shifts to orbits with even lower angular momenta, $j_z/j_c \approx 0.2$, and a larger fraction of counter-rotating orbits as expected in spheroids.

Heating of stellar orbits is, however, not in conflict with observations of dIrrs since they are characterized by thick stellar discs with small v/σ ratios. To quantify the amount of orbital heating due to radiative feedback relative to observed dwarf galaxies, we compare the total angular momentum content of the simulations to robust estimates from observations. Romanowsky & Fall (2012) performed a thorough analysis of the total angular momentum content of galaxies as a function of luminosity and morphological type. They find a clear trend of increasing specific angular momentum with increasing stellar mass as well as for later Hubble types at a fixed stellar mass. The data for late-type galaxies can be fit using the relation $\log j_* = \log j_0 + \alpha[\log(M_*/\mathrm{M}_\odot) - 11.0]$, with $\log j_0 = 3.11$, $\alpha = 0.53$ and $\sigma_{\log j_*} = 0.22$. The total angular momentum within 5 kpc in our galaxies simulated with full radiative feedback is $j_* \approx 45\,\mathrm{kpc\,km\,s^{-1}}$ for the fiducial model, $j_* \approx 28\,\mathrm{kpc\,km\,s^{-1}}$ for `dwALL_8`, and $j_* \approx 21\,\mathrm{kpc\,km\,s^{-1}}$ for `dwALL_40`. These are in good agreement with predictions from the fit to observations, $j_* = 38^{+25}_{-15}$, $14.5^{+9.5}_{-5.8}\,\mathrm{kpc\,km\,s^{-1}}$ for `dwALL_1` and `dwALL_8`, respectively. The simulation with the largest photoheating pressure, `dwALL_40`, contains more angular momentum than the extrapolation from the observations.

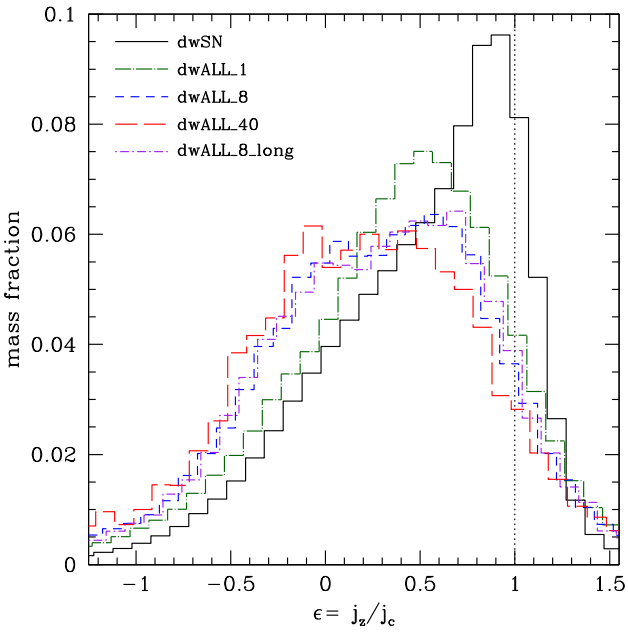

Figure 13. Mass-weighted distribution of stellar orbital circularity, $\epsilon \equiv j_z/j_c$, where j_z is the specific angular momentum of the stars along the rotation axis of the cold gas disc and j_c is the specific angular momentum of a circular orbit at the same radius. The vertical line marks the location of a circular orbit. Only simulations at $z = 0$ are shown. Radiation feedback shifts the peak of the distribution towards $\epsilon \sim 0.5$ and increases the fraction of stars in non-circular and counter-rotating orbits. Runs with larger photoheating values have broader distributions with larger dispersion support.

Observations provide much tighter constraints on the stellar distribution of disc galaxies. For the MW, the ratio of disc scaleheight to exponential length is ∼0.1 (Gilmore & Reid 1983), while nearby late-type galaxies have ratios $\lesssim 0.2$ in the R band (Yoachim & Dalcanton 2006). For the `spALL_40` simulation at $z = 0.2$, Fig. 14 shows the distribution of orbital circularity. In this case, strong radiation feedback causes 60 per cent of stars to have non-circular orbits. As expected, the left-hand panel of Fig. 14, shows that younger stars have a greater degree of rotational support. Typically, in the literature, simulations with a large fraction of stars near $j_z/j_c \approx 0$ have a prominent bulge which contains essentially all of the low-circularity stars. Interestingly, this is not the case in our simulations with radiative feedback. Instead, in our experiments, the non-rotational component of the galaxy seems to be a part of the stellar disc. This is evident in the right-hand panel of Fig. 14, where we compare the circularity distribution of stars located outside a projected radius 2, 5 and 7 kpc to remove any possible contribution from a central bulge. Even when only the disc stars are considered, the pressure supported component remains.

Fig. 15 shows the projected luminosity density of the galaxy in both face-on and edge-on projections in the U and I band at $z = 0.2$. The mass-to-light ratios were obtained using the `CMD2.5` stellar evolution code (Marigo et al. 2008). No central spheroidal component is visible in the infrared edge-on image.

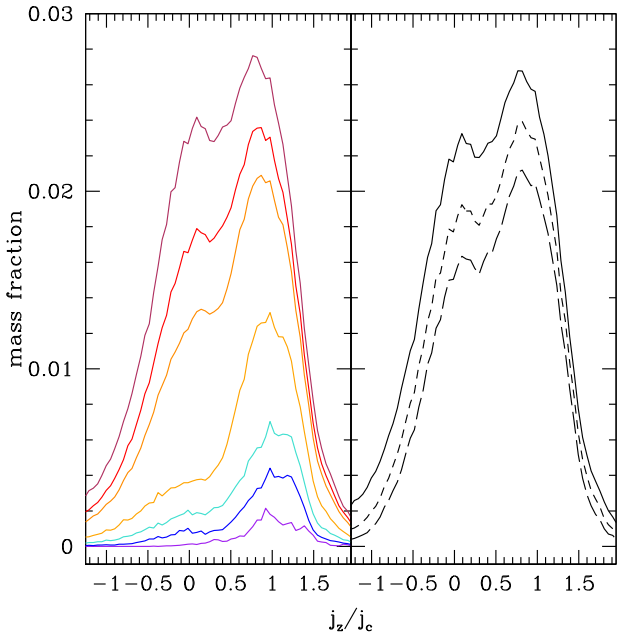

Figure 14. Mass-weighted distribution of stellar orbital circularity for `spALL_40` at $z = 0.2$. Left: from top to bottom, the curves show stars with ages <12, 5, 4, 2, 1, 0.5, 0.05 Gyr. Right: effect of removing the innermost stars. All ages are included. Solid, short-dashed and long-dashed curves show only stars with $r > 2$, 5, 7 kpc, respectively. About 40 per cent of the stellar mass of the galaxy is in a thickened disc component with non-circular orbits that is composed mostly of stars older than ∼4 Gyr. There is no sign of a central dispersion-supported bulge. Only the youngest stars have predominantly circular orbits.

To examine the structure of the `spALL_40` model, we fit the radial and vertical surface brightness in the *R* band with exponential profiles. The results are shown in Fig. 16. In agreement with the images, the face-on radial profile is fit entirely by a pure exponential, indicating the absence of a bulge. In addition, the disc shows a truncation at $r \approx 25$ kpc. The exponential length in the *R* band is $r_d = 5.8$ kpc, and the scaleheight measured between 6 and 9 kpc is $z_d = 1.1$ kpc, giving a ratio $z_d/r_d = 0.19$. This ratio is consistent with observations and shows that the simulated galaxy is simply more extended than real galaxies in every dimension. We checked the thickness of the star-forming disc in `spALL_40` by fitting the vertical mass profile of the stars with ages <10 Myr. The star-forming disc has a scaleheight ≈400 pc, or about 5–8 times thicker than molecular gas in the MW.

5.5.1 *Discussion*

We have shown that radiation from massive stars significantly affects the distribution of stellar orbits in low-mass galaxies in numerical experiments. However, the effect is opposite to what is observed in other simulations with efficient stellar feedback (Governato et al. 2010; Guedes et al. 2011; Brook et al. 2012), where higher resolution and delayed cooling result in more disc-dominated galaxies. When comparing the SN and the fiducial radiation feedback model, we find that the amount of stars in circular orbits with only SNe feedback is much larger. RP increases the amount of random motions in the stellar component and the effect is exacerbated for models with increased photoheating pressure ($P_{PH} > 10^6$ K cm^{-3}). In contrast with previous works, our low-mass spiral galaxy with is bulgeless and stars in orbits with low circularity are part of the disc.

In the last decade, many works have focused on the effect of strong SNe feedback on the morphology of low-mass galaxies. Governato et al. (2010) show that the distribution of angular momentum in SPH simulations of a dwarf galaxy with $M_* = 4.8 \times 10^8$ M$_\odot$ and thermal feedback with delayed cooling agrees well with observational estimates (e.g. van den Bosch, Burkert & Swaters 2001). Furthermore, Christensen et al. (2014) show that including a more physical SF prescription in the same simulations preserves the agreement. Despite the difficulty in directly measuring the distribution of orbital circularity in observations, Governato et al. (2007) show that tuning the amount of energy from SN that couples to the gas may dramatically increase the dominance of circular orbits in simulations.

In a more recent paper, Roškar et al. (2014) argue that including radiation feedback in adaptive mesh simulations of the formation of a MW-analogue helps to regulate the SFR at high redshift. However, this occurs at the expense of creating a kinematically hot disc with a large stellar velocity dispersion. Our results are consistent with Roškar et al. (2014) and indicate that there is a limit to the rotational support of the disc when radiation from massive stars is included. For larger forcing due to increased photoheating in H II regions, low-mass galaxies show increased support from random motions. This is likely due to the larger velocity dispersion of the star-forming ISM due radiative feedback. This result might indicate the need to include additional physics in the simulations, or it may simply show that our spatial resolution (50–100 pc or about the scaleheight of the O stars in the MW) is insufficient to produce a thin disc. It may also indicate that large values of radiative forcing do not occur in nature. Our results also indicate that our discs are not only too thick but also overextended. SF at large galactocentric distances could be reduced by, for example, increasing the gas density threshold for SF. However, a thorough comparison should be carried out before ruling out observational effects. This should include, for instance, performing disc fits of mock observations which include the appropriate observational systematics.

5.6 How does radiation regulate SF?

In this section, we investigate the properties of the gas in the simulations in order to establish the link between radiative feedback and stellar mass assembly. We begin by calculating the distribution of the gas in the galaxy as a function of density and temperature. Fig. 17 shows the distribution of gas mass as a function of density and temperature in the ISM of the galaxy ($r < 5$ kpc). The distribution of gas in phase space is similar in all the models, with most of the mass in a narrow locus where feedback heating balances radiative cooling near 10^4 K. Below this temperature, a cold and dense phase with $n > 0.1$ cm^{-3} is observed. Above 10^4 K, there is typically a broad tail of warm/hot, very dilute gas. While all the models with RP and photoheating have similar ISM distributions, simulations with SN feedback contain a large fraction of gas mass in the cold, dense phase where it forms stars actively. This large cold gas reservoir causes the high SFR in Fig. 9 as well as the large baryon fraction within the galaxy in Fig. 6. In sharp contrast, models with full radiation feedback are able to disrupt star-forming gas clouds soon after the first stars are formed, preventing a further increase in the gas density of the ISM of the galaxy. This process greatly reduces the amount of dense and cold gas in the tail of the distribution observed in the fiducial radiation feedback run compared to the `dwSN` model. The phase plot for `dwALL_1` indicates that a large fraction of the cold and dense ISM ($n > 0.5$ cm^{-3}, $T < 10^4$ K) gas

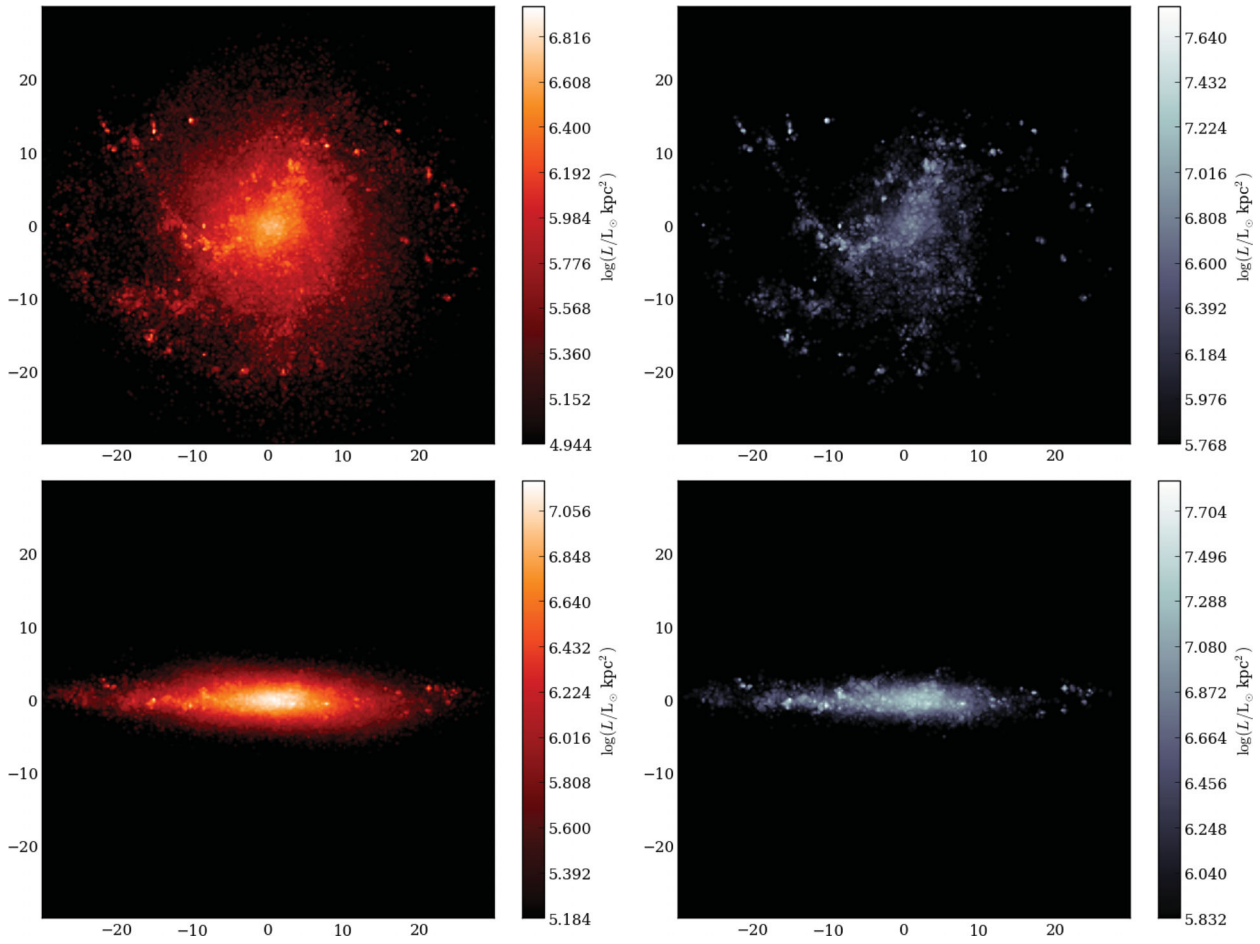

Figure 15. Integrated line-of-sight luminosity for face-on and edge-on projections for `spALL_40` at $z = 0.2$. Left: I band. Right: U band. Scales are in kiloparsecs. Radiation feedback prevents the formation of a bulge in a low-mass spiral. However, the stellar disc is too large in both radius and height. The thickening is apparent even in the young stars that dominate the UV flux, showing that stars are born far from the plane due to radiation-induced turbulence in the ISM. Luminosities were obtained using the `CMD2.5` stellar evolution code (Marigo et al. 2008) and assume solar metallicity.

mass that would otherwise be quickly converted to stars is diluted and expelled from the galaxy.

Radiation from massive stars is capable of dramatically reducing the amount of gas that forms stars by dispersing dense and cold gas clumps that surround star-forming regions. During SF bursts in dwarf runs the dense ISM is destroyed and SF is halted in the entire galaxy as observed in Fig. 9. As shown in Fig. 6, a large fraction of this gas is expelled from the galaxy by means of overpressured bubbles around young star clusters. In simulations, where the photoheating pressure is assumed to be larger, depletion of the ISM is greater across all phases. In a forthcoming paper, we discuss the nature of these gas flows and their effect on the CGM.

5.6.1 Discussion

In recent works, Stinson et al. (2013) and Brook et al. (2012) used a combination of delayed cooling and an increase of a factor of $\sim$10 in the thermal SN energy (compared to the canonical value of $\sim 10^{51}$ erg) in cosmological galaxy simulations. This extreme 'early feedback' led to a reduction in the stellar mass growth of galaxies at high redshift. For galaxies with masses $M_{\rm vir} = 3$–$20 \times 10^{10}\,{\rm M}_{\odot}$, the simulations presented here have similar SFHs which are in excellent agreement with semi-empirical models and archaeological observations of nearby dwarfs. However, as shown in Fig. 17, and in Section 5.6, radiative feedback can effectively disperse and expel cold and dense gas without heating it beyond $\sim 10^5$ K. With the delayed cooling used in the 'blastwave' approximation temperatures in star forming gas reach $\sim 2 \times 10^7$ K for several million years. In fact, in controlled isolated simulations of a massive spiral galaxy, Agertz et al. (2013) demonstrate that thermal energy injection with delayed cooling produces about 100 times more gas above 10^4 K in the ISM than momentum from radiation, even if both are able to regulate the SFR.

If hot gas was responsible for the regulation of the SFR it would be ubiquitous around galactic young star clusters. However, observations of nearby evolved H II regions detect a negligible volume fraction of hot X-ray emitting gas (Lopez et al. 2011, 2014), showing that the effect of shock-heating by SN and stellar winds is short-lived. Lopez et al. (2011) and Lopez et al. (2014) also estimate the dynamical effect of the observed X-ray gas and find that it is negligible in the context of the dispersal of the molecular cloud. These observations strengthen the argument against the regulation of the SF in galaxies by large SNe blastwaves that remain at $T > 10^7$ K for several million years. In this paper, we have shown that the combination of radiation momentum and photoionization heating is instead a more viable physical mechanism to explain the slow rate of stellar mass growth of low-mass galaxies at $z > 1$.

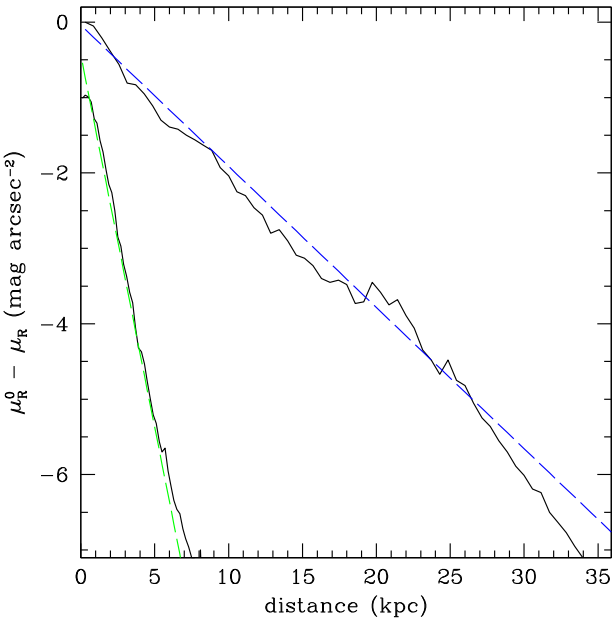

Figure 16. Radial (upper curve) and vertical (lower curve) *R*-band surface brightness profiles for `spALL_40`. Dashed lines show exponential fits. The vertical profile is calculated at $6 < r < 9$ kpc. Both the radial and the vertical profiles are well fitted by a pure exponential. The disc is truncated at ≈25 kpc.

6 CONCLUSIONS

We have for the first time analysed the full effects of radiation from massive stars on the formation of low-mass galaxies in cosmological hydrodynamic simulations. In contrast with other works, we explicitly included the important contribution of photoionization heating in H II regions in addition to radiation momentum. We find the following.

(i) The local efficiency of SF observed in nearby star clusters is not sufficiently high to destroy the parent clouds with energy from SNe and stellar winds. However, radiation momentum and photoionization heating overpressure gas and cause it to expand, quickly dispersing the parent gas cloud (Section 3).

(ii) The fraction of baryons that condense to form a low-mass galaxy with radiative feedback is ∼7 per cent, about half of the universal fraction, and slightly larger than the baryonic fraction in a galaxy formed with SN feedback alone. This surprising result indicates that stellar radiation may not be important in ejecting large amounts of gas from the halo. Instead, it acts to regulate the early SFR by dispersing cold and dense gas for several million years (Fig. 17).

(iii) Stellar radiation regulates the SF in isolated dwarf and low-mass spiral galaxies at all epochs, but especially at $z > 1$, where it reduces the SFR by 2 orders of magnitude compared to SN explosions alone. The SFHs of simulated dwarfs with radiative feedback are constant or increasing with time, a feature observed in nearby dwarfs that had until now eluded analytical models and simulations. The growth of the stellar mass of a spiral galaxy with $M_{\rm vir} = 2 \times 10^{11}$ M$_\odot$ also matches semi-empirical and observational estimates (Fig. 9).

(iv) Radiation feedback (mainly due to photoheating) works by delaying the conversion of newly accreted gas into stars, and keeps gas in a reservoir to fuel SF at $z \lesssim 1$. This mechanism decouples the assembly of the galaxy from the hierarchical growth of the host DM halo (Fig. 7). The sSFR of runs that include radiation momentum and photoheating agree with direct observational estimates at $z = 0$ and 1 (Section 5.2.1), and with the archaeological data from Weisz et al. (2014, Fig. 8). Radiation feedback may thus play an important role in producing the phenomenon of galaxy downsizing in sub-$L^\star$ galaxies.

(v) Low-efficiency SF reduces the SNe energy per unit gas mass (Fig. 2) and leads to catastrophic overcooling and circular velocity curves that peak at small radii and decline quickly. Pressure from stellar radiation and photoheating overcomes self-gravity and disperses cold gas to prevent overcooling (Fig. 3). This produces circular velocity curves that rise slowly and are DM-dominated, in excellent agreement with observations of nearby dIrrs (Fig. 10 and Section 5). Our simulated spiral galaxy shows no sign of a central

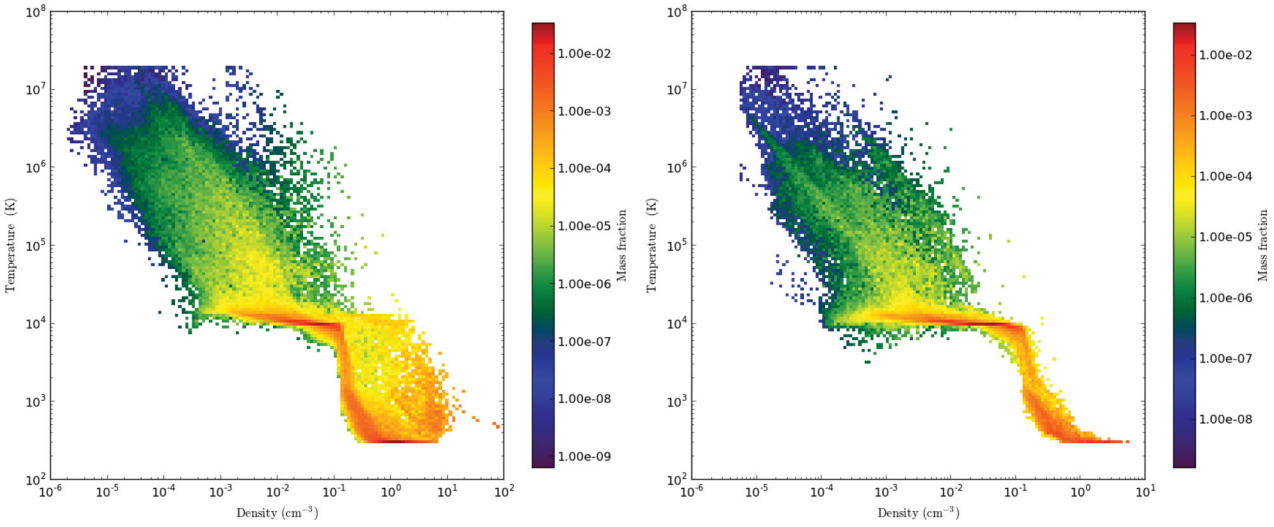

Figure 17. Density–temperature phase-space distribution of gas mass in dwarf simulations at $z = 0$. Only gas contained within a sphere of radius 5 kpc around the centre of the galaxy is shown. Left: `dwSN`. Right: `dwALL_8`. Radiation feedback from massive stars prevents the accumulation of gas in the cold and high-density tail of the distribution, leading to a reduction of the SFR and ejection of gas from the galaxy. The figure was prepared using the `yt` analysis and visualization package (Turk et al. 2011).

bulge in either surface brightness maps (Figs 15 and 16), or in the stellar kinematics (Fig. 14).

(vi) Dwarf galaxies simulated with radiative feedback have bursty SFHs, with larger and more frequent bursts at $z < 1$. This is in contrast with models with only SN energy, where the largest bursts occur near the peak of the SFH, at $z \sim 2$ (Fig. 9). Bursty SF leads to a reduction in the DM density in the central $\sim$1 kpc compared to a run without baryons (Fig. 11). The density and slope agree with estimates from observations of galaxies of the same mass, and confirms the ability of stellar radiation to alter the distribution of DM without the need to artificially increase the SN efficiency. The effect is much smaller in a low-mass spiral galaxy at $z \sim 1$.

(vii) Stellar radiation increases the height of the stellar disc in a low-mass spiral. Although the ratio of scaleheight to exponential length fits observations, the scaleheight of the star-forming disc is 5–8 times greater than in the MW. The thickened disc causes the fraction of stars in circular orbits in the galaxy to decrease by a factor of $\gtrsim$2 compared to simulations with only SNe energy. These tensions may be resolved by increasing the SF density threshold in the simulations.

ACKNOWLEDGEMENTS

We would like to thank the referee for valuable and insightful suggestions which greatly improved the paper. We also thank Mark Krumholz, Oscar Agertz and Andrey Kravtsov for illuminating discussions, as well as Peter Behroozi for providing his data. ST, AK and JP were supported by grant STSci/HST-AR-12647.01, NSF grant NSF-AST-1010033, as well as the collaborative grant NSF-AST-1009908. This work was partially supported by MINECO (Spain) - AYA2012-31101 and MICINN (Spain) AYA-2009-13875-C03-02. DC is a Juan de la Cierva fellow. KA was supported by the National Science Foundation under Grant No. DGE-1144468. All the simulations were performed at the National Energy Research Scientific Computing Center, which is supported by the Office of Science of the US Department of Energy under Contract No. DE-AC02-05CH11231.

REFERENCES

Adams J. J., Gebhardt K., Blanc G. A., Fabricius M. H., Hill G. J., Murphy J. D., van den Bosch R. C. E., van de Ven G., 2012, ApJ, 745, 92
Adams J. J. et al., 2014, ApJ, 789, 63
Agertz O., Teyssier R., Moore B., 2011, MNRAS, 410, 1391
Agertz O., Kravtsov A. V., Leitner S. N., Gnedin N. Y., 2013, ApJ, 770, 25
Andrews B. H., Thompson T. A., 2011, ApJ, 727, 97
Avila-Reese V., Colín P., González-Samaniego A., Valenzuela O., Firmani C., Velázquez H., Ceverino D., 2011, ApJ, 736, 134
Baldry I. K., Glazebrook K., Brinkmann J., Ivezić Ž., Lupton R. H., Nichol R. C., Szalay A. S., 2004, ApJ, 600, 681
Behroozi P. S., Conroy C., Wechsler R. H., 2010, ApJ, 717, 379
Behroozi P. S., Wechsler R. H., Conroy C., 2013, ApJ, 770, 57
Bigiel F., Leroy A., Walter F., Brinks E., de Blok W. J. G., Madore B., Thornley M. D., 2008, AJ, 136, 2846
Blais-Ouellette S., Amram P., Carignan C., Swaters R., 2004, A&A, 420, 147
Blanton M. R. et al., 2003, ApJ, 594, 186
Blumenthal G. R., Faber S. M., Flores R., Primack J. R., 1986, ApJ, 301, 27
Brook C. B. et al., 2011, MNRAS, 415, 1051
Brook C. B., Stinson G., Gibson B. K., Wadsley J., Quinn T., 2012, MNRAS, 424, 1275
Brook C. B., Stinson G., Gibson B. K., Shen S., Macciò A. V., Wadsley J., Quinn T., 2014, MNRAS, 443, 3809
Brooks A. M., Governato F., Booth C. M., Willman B., Gardner J. P., Wadsley J., Stinson G., Quinn T., 2007, ApJ, 655, L17
Calura F. et al., 2012, MNRAS, 427, 1401
Ceverino D., Klypin A., 2009, ApJ, 695, 292
Ceverino D., Dekel A., Bournaud F., 2010, MNRAS, 404, 2151
Ceverino D., Klypin A., Klimek E., Trujillo-Gomez S., Churchill C. W., Primack J., Dekel A., 2014, MNRAS, 442, 1545
Christensen C. R., Governato F., Quinn T., Brooks A. M., Shen S., McCleary J., Fisher D. B., Wadsley J., 2014, MNRAS, 440, 2843
Colín P., Vázquez-Semadeni E., Gómez G. C., 2013, MNRAS, 435, 1701
Dale J. E., Ercolano B., Bonnell I. A., 2012, MNRAS, 424, 377
Davis S. W., Jiang Y.-F., Stone J. M., Murray N., 2014, preprint (arXiv:1403.1874)
de Blok W. J. G., McGaugh S. S., 1997, MNRAS, 290, 533
de Blok W. J. G., McGaugh S. S., Bosma A., Rubin V. C., 2001, ApJ, 552, L23
De Rossi M. E., Avila-Reese V., Tissera P. B., González-Samaniego A., Pedrosa S. E., 2013, MNRAS, 435, 2736
Di Cintio A., Brook C. B., Macciò A. V., Stinson G. S., Knebe A., Dutton A. A., Wadsley J., 2014, MNRAS, 437, 415
Duffy A. R., Schaye J., Kay S. T., Dalla Vecchia C., Battye R. A., Booth C. M., 2010, MNRAS, 405, 2161
Dunne L. et al., 2009, MNRAS, 394, 3
Dutton A. A., 2009, MNRAS, 396, 121
Dutton A. A., Conroy C., van den Bosch F. C., Prada F., More S., 2010, MNRAS, 407, 2
Dutton A. A. et al., 2011, MNRAS, 416, 322
Firmani C., Avila-Reese V., 2010, ApJ, 723, 755
Firmani C., Avila-Reese V., Rodríguez-Puebla A., 2010, MNRAS, 404, 1100
Flores R. A., Primack J. R., 1994, ApJ, 427, L1
Fukugita M., Hogan C. J., Peebles P. J. E., 1998, ApJ, 503, 518
Geha M., Blanton M. R., Yan R., Tinker J. L., 2012, ApJ, 757, 85
Genel S. et al., 2012, ApJ, 745, 11
Gilbank D. G. et al., 2011, MNRAS, 414, 304
Gilmore G., Reid N., 1983, MNRAS, 202, 1025
Gnedin O. Y., Kravtsov A. V., Klypin A. A., Nagai D., 2004, ApJ, 616, 16
Gnedin O. Y., Ceverino D., Gnedin N. Y., Klypin A. A., Kravtsov A. V., Levine R., Nagai D., Yepes G., 2011, preprint (arXiv:e-prints)
González-Samaniego A., Colín P., Avila-Reese V., Rodríguez-Puebla A., Valenzuela O., 2014, ApJ, 785, 58
Governato F., Willman B., Mayer L., Brooks A., Stinson G., Valenzuela O., Wadsley J., Quinn T., 2007, MNRAS, 374, 1479
Governato F. et al., 2010, Nature, 463, 203
Governato F. et al., 2012, MNRAS, 422, 1231
Guedes J., Callegari S., Madau P., Mayer L., 2011, ApJ, 742, 76
Guo Q., White S., Li C., Boylan-Kolchin M., 2010, MNRAS, 404, 1111
Haas M. R., Schaye J., Booth C. M., Dalla Vecchia C., Springel V., Theuns T., Wiersma R. P. C., 2013, MNRAS, 435, 2931
Hoare M. G., Kurtz S. E., Lizano S., Keto E., Hofner P., 2007, in Reipurth V. B., Jewitt D., Keil K., eds, Protostars and Planets V. Univ. Arizona Press, Tucson, p. 181
Hoekstra H., Hsieh B. C., Yee H. K. C., Lin H., Gladders M. D., 2005, ApJ, 635, 73
Hopkins P. F., Quataert E., Murray N., 2011, MNRAS, 417, 950
Hopkins P. F., Kereš D., Oñorbe J., Faucher-Giguère C.-A., Quataert E., Murray N., Bullock J. S., 2014, MNRAS, 445, 581
Indebetouw R. et al., 2009, ApJ, 694, 84
Jiang G., Kochanek C. S., 2007, ApJ, 671, 1568
Karim A. et al., 2011, ApJ, 730, 61
Kawamura A. et al., 2009, ApJS, 184, 1
Kennicutt R. C., Jr, 1998, ApJ, 498, 541
Klypin A., Prada F., Yepes G., Hess S., Gottlober S., 2013, preprint (arXiv:e-prints)
Kravtsov A. V., 1999, PhD thesis, New Mexico State University
Kravtsov A. V., Klypin A. A., Khokhlov A. M., 1997, ApJS, 111, 73
Krumholz M. R., Matzner C. D., 2009, ApJ, 703, 1352
Krumholz M. R., Tan J. C., 2007, ApJ, 654, 304

Krumholz M. R., Thompson T. A., 2012, ApJ, 760, 155
Kuzio de Naray R., McGaugh S. S., Mihos J. C., 2009, ApJ, 692, 1321
Leauthaud A. et al., 2012, ApJ, 744, 159
Leitherer C. et al., 1999, ApJS, 123, 3
Leitner S. N., 2012, ApJ, 745, 149
Lopez L. A., Krumholz M. R., Bolatto A. D., Prochaska J. X., Ramirez-Ruiz E., 2011, ApJ, 731, 91
Lopez L. A., Krumholz M. R., Bolatto A. D., Prochaska J. X., Ramirez-Ruiz E., Castro D., 2014, ApJ, 795, 121
Macciò A. V., Stinson G., Brook C. B., Wadsley J., Couchman H. M. P., Shen S., Gibson B. K., Quinn T., 2012, ApJ, 744, L9
McConnachie A. W., 2012, AJ, 144, 4
Madau P., Weisz D. R., Conroy C., 2014, ApJ, 790, L17
Mandelbaum R., Seljak U., Kauffmann G., Hirata C. M., Brinkmann J., 2006, MNRAS, 368, 715
Marigo P., Girardi L., Bressan A., Groenewegen M. A. T., Silva L., Granato G. L., 2008, A&A, 482, 883
Mashchenko S., Wadsley J., Couchman H. M. P., 2008, Science, 319, 174
Mateo M. L., 1998, ARA&A, 36, 435
Miller S. H., Ellis R. S., Newman A. B., Benson A., 2014, ApJ, 782, 115
Moore B., 1994, Nature, 370, 629
Moster B. P., Naab T., White S. D. M., 2013, MNRAS, 428, 3121
Munshi F. et al., 2013, ApJ, 766, 56
Murray N., 2011, ApJ, 729, 133
Murray N., Quataert E., Thompson T. A., 2010, ApJ, 709, 191
Murray N., Ménard B., Thompson T. A., 2011, ApJ, 735, 66
Noeske K. G. et al., 2007, ApJ, 660, L43
Oh S.-H., de Blok W. J. G., Walter F., Brinks E., Kennicutt R. C., Jr, 2008, AJ, 136, 2761
Oh S.-H., de Blok W. J. G., Brinks E., Walter F., Kennicutt R. C., Jr, 2011a, AJ, 141, 193
Oh S.-H., Brook C., Governato F., Brinks E., Mayer L., de Blok W. J. G., Brooks A., Walter F., 2011b, AJ, 142, 24
Oppenheimer B. D., Davé R., 2008, MNRAS, 387, 577
Oppenheimer B. D., Davé R., Kereš D., Fardal M., Katz N., Kollmeier J. A., Weinberg D. H., 2010, MNRAS, 406, 2325
Pellegrini E. W., Baldwin J. A., Ferland G. J., 2011, ApJ, 738, 34
Pontzen A., Governato F., 2012, MNRAS, 421, 3464
Rhee G., Valenzuela O., Klypin A., Holtzman J., Moorthy B., 2004, ApJ, 617, 1059
Rodighiero G. et al., 2010, A&A, 518, L25
Rodríguez-Puebla A., Drory N., Avila-Reese V., 2012, ApJ, 756, 2
Romanowsky A. J., Fall S. M., 2012, ApJS, 203, 17
Roškar R., Teyssier R., Agertz O., Wetzstein M., Moore B., 2014, MNRAS, 444, 2837
Salim S. et al., 2007, ApJS, 173, 267
Scannapieco C. et al., 2012, MNRAS, 423, 1726
Shen S., Madau P., Guedes J., Mayer L., Prochaska J. X., Wadsley J., 2013, ApJ, 765, 89
Shen S., Madau P., Conroy C., Governato F., Mayer L., 2014, ApJ, 792, 99
Simon J. D., Bolatto A. D., Leroy A., Blitz L., Gates E. L., 2005, ApJ, 621, 757
Somerville R. S. et al., 2008, ApJ, 672, 776
Stinson G., Seth A., Katz N., Wadsley J., Governato F., Quinn T., 2006, MNRAS, 373, 1074
Stinson G. S., Bailin J., Couchman H., Wadsley J., Shen S., Nickerson S., Brook C., Quinn T., 2010, MNRAS, 408, 812
Stinson G. S., Brook C., Macciò A. V., Wadsley J., Quinn T. R., Couchman H. M. P., 2013, MNRAS, 428, 129
Teyssier R., Pontzen A., Dubois Y., Read J. I., 2013, MNRAS, 429, 3068
Tissera P. B., White S. D. M., Pedrosa S., Scannapieco C., 2010, MNRAS, 406, 922
Truelove J. K., Klein R. I., McKee C. F., Holliman J. H., II, Howell L. H., Greenough J. A., 1997, ApJ, 489, L179
Trujillo-Gomez S., Klypin A., Primack J., Romanowsky A. J., 2011, ApJ, 742, 16
Turk M. J., Smith B. D., Oishi J. S., Skory S., Skillman S. W., Abel T., Norman M. L., 2011, ApJS, 192, 9
van den Bosch F. C., Burkert A., Swaters R. A., 2001, MNRAS, 326, 1205
Vogelsberger M., Genel S., Sijacki D., Torrey P., Springel V., Hernquist L., 2013, MNRAS, 436, 3031
Weinmann S. M., Pasquali A., Oppenheimer B. D., Finlator K., Mendel J. T., Crain R. A., Macciò A. V., 2012, MNRAS, 426, 2797
Weisz D. R. et al., 2011a, ApJ, 739, 5
Weisz D. R. et al., 2011b, ApJ, 743, 8
Weisz D. R. et al., 2012, ApJ, 744, 44
Weisz D. R., Dolphin A. E., Skillman E. D., Holtzman J., Gilbert K. M., Dalcanton J. J., Williams B. F., 2014, ApJ, 789, 147
Whitaker K. E., van Dokkum P. G., Brammer G., Franx M., 2012, ApJ, 754, L29
Yoachim P., Dalcanton J. J., 2006, AJ, 131, 226

APPENDIX A: THE KENNICUTT–SCHMIDT RELATION USING LOCAL SF

The SF model used here is based on the observed local efficiency of conversion of gas into stars in molecular clouds that are typically less than 100 pc in size. This does not guarantee that the global relation between gas density and SFR will follow the Kennicutt–Schmidt law (Kennicutt 1998) on global galactic scales. Fig. A1 shows the surface density of SF as a function of cold gas surface density for several runs. Here, gas with temperature $T < 15\,000$ K is considered cold, and density is projected inside a 1 kpc tall cylinder oriented along the total angular momentum vector of the young stars in each case. Each symbol in Fig. A1 represents an azimuthal average in a 1 kpc annulus at a different radius. The figure also reproduces the original fit to global spiral and starburst galaxy data by Kennicutt

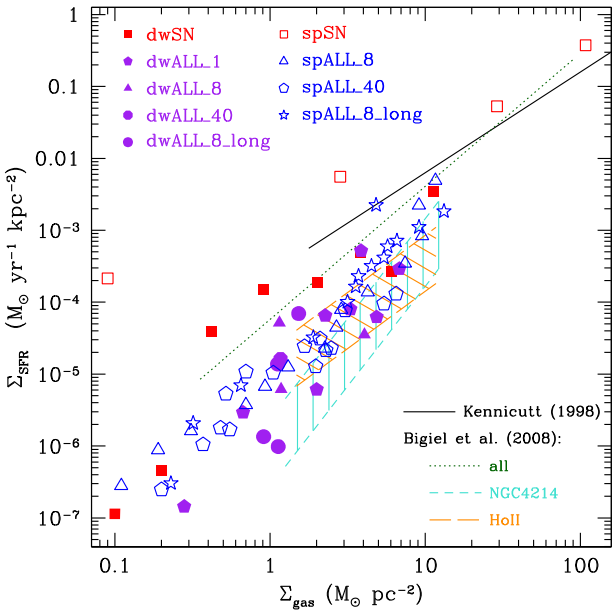

Figure A1. Surface density of SF versus surface density of cold gas with $T < 15\,000$ K. Filled symbols represent `dwarf` models and open symbols represent the `spiral` runs. The projection is performed on to a plane of thickness 1 kpc defined by the angular momentum vector of the cold gas disc. Different points for each model show the azimuthal averages in 1 kpc annuli at various galactocentric distances. The solid line is the fit to local spirals from Kennicutt (1998), while the dotted line show the fit to spirals and irregulars from Bigiel et al. (2008), and the hatched areas represent the fits and scatter for two individual dwarf irregular galaxies. Our local model of SF results in simulated dwarfs that successfully reproduce observations of individual dIrrs. Stellar RP tends to reduce the SFR surface density compared to SNe energy alone.

(1998) and the recent fit to 750 pc patches in spirals and dIrrs by Bigiel et al. (2008). In addition, we plot the fit and 1σ scatter of individual sets of measurements in 750 pc apertures throughout two dIrrs, NGC 4214 and HoII, from Bigiel et al. (2008).

Qualitatively, all our simulated dwarf galaxies show overall agreement with the normalization and the slope of the Kennicutt–Schmidt relation. Moreover, it is remarkable that using only a local deterministic SF prescription, we reproduce the observed Kennicutt–Schmidt relation on galactic scales. For dwarf runs, the effect on the relation of including additional feedback physics is relatively small. However, the relation between SFR and cold gas surface density for the simulated spiral galaxies with only SN energy lies well above the points for models that include radiation feedback from massive stars. The overall slope of the simulations that include radiation is also generally steeper than those with only SN feedback. SF in galaxies that incorporate radiation momentum and photoheating pressure seems to proceed at a slower rate for any given value of cold gas column density, and this behaviour is more marked at low gas surface densities near the observational detection thresholds, $\Sigma_{\rm gas} \lesssim 3\ {\rm M}_{\odot}\ {\rm pc}^{-2}$. In addition to reducing the SFR density, radiation from massive stars also decreases the maximum column density reached by cold gas in the ISM.

This paper has been typeset from a TEX/LATEX file prepared by the author.